HHS Public Access

Author manuscript

Biomaterials. Author manuscript; available in PMC 2019 May 06.

Published in final edited form as:

Biomaterials. 2018 March ; 157: 62–75. doi:10.1016/j.biomaterials.2017.12.002.

Optical molecular imaging for tumor detection and image-guided surgery

Chensu Wang[a,b], **Zhaohui Wang**[a], **Tian Zhao**[a], **Yang Li**[a], **Gang Huang**[a], **Baran D. Sumer**[c,**], and **Jinming Gao**[a,c,*]

[a]Department of Pharmacology, Simmons Comprehensive Cancer Center, University of Texas Southwestern Medical Center, 5323 Harry Hines Blvd., Dallas, TX 75390, USA

[b]Department of Cell Biology, University of Texas Southwestern Medical Center, 5323 Harry Hines Blvd., Dallas, TX 75390, USA

[c]Department of Otolaryngology, University of Texas Southwestern Medical Center, 5323 Harry Hines Blvd., Dallas, TX 75390, USA

Abstract

We have witnessed rapid development of fluorescence molecular imaging of solid tumors for cancer diagnosis and image-guided surgery in the past decade. Many biomarkers unique to cancer cells or tumor microenvironment, such as cell surface receptors, hypoxia, secreted proteases and extracellular acidosis have been characterized, and can be used to distinguish cancer from normal tissue. A variety of optical imaging probes have been developed to target these biomarkers to improve tumor contrast over the background tissue. Unlike conventional anatomical and molecular imaging technologies, fluorescent imaging method benefits from its safety, high-spatial resolution and real-time capability, and therefore, has become a highly adoptable imaging method for tumor detection and image-guided surgery in clinics. In this review, we summarize recent progress in 'always-ON' and stimuli-activatable fluorescent imaging probes, and discuss their potentials in tumor detection and image-guided surgery.

Keywords

Cancer molecular imaging; Stimuli-responsive nanomaterials; Tumor microenvironment; Cancer diagnosis; Image-guided surgery

1. Introduction

Cancer is a leading cause of death worldwide. In 2016, there were 1,685,210 new cancer cases and 595,690 deaths in the U.S. The lifetime risk for developing cancer is approximately 40% [1]. In addition to chemotherapy and radiation therapy, oncologic surgery represents one of the cornerstones of therapy, with over 80% of cancer patients undergoing surgery as part of their treatment [2,3]. Often for patients with solid cancers,

*Corresponding author. Department of Pharmacology, Simmons Comprehensive Cancer Center, University of Texas Southwestern Medical Center, 5323 Harry Hines Blvd., Dallas, TX 75390, USA. **Corresponding author. baran.sumer@utsouthwestern.edu (B.D. Sumer), jinming.gao@utsouthwestern.edu (J. Gao).

surgery is the only curative option. Successful oncologic surgery is predicated on accurate visualization of the cancer so that precise removal with minimal damage to normal tissues can be achieved.

Modern imaging methods have revolutionized medicine including cancer diagnosis and therapy. The development of ultrasound, magnetic resonance imaging (MRI) and computed tomography (CT) have allowed physicians to more precisely screen patients for cancer and localize lesions. These techniques also guide surgery and the delivery of radiotherapy improving precision, and allow non-invasive monitoring of patients' response to therapy. However, current clinical imaging techniques mostly reveal differences in anatomic structures and do not cue off tumor specific signals except in some limited cases, such as positron emission tomography with ^{18}F-flurodeoxyglucose (FDG-PET) and radioactive iodine imaging for well differentiated thyroid cancer. They also do not provide real-time imaging during radiotherapy or surgery, with patients requiring treatment interruption for high resolution imaging. These modalities are also expensive and cumbersome, requiring expensive installation of specific instruments in the operating room (OR), which only provide marginal benefits over conventional surgical navigation [4].

Rapid technological advances over the last few years have enabled the mainstream use of optical imaging strategies to image tissues intra-operatively based on cellular imaging, native autofluorescence, and Raman scattering [5–11]. The potential advantages of optical imaging include real-time feedback and the availability of relatively inexpensive camera systems that provide a wide view of the surgical field. More importantly, optical imaging augments the natural visualization technique used by surgeons with easy incorporation into the normal clinical flow of surgery. As a result, a variety of fluorophores targeting tumors at molecular and cellular levels have been developed for image-guided surgery. Most of these strategies focus on cancer specific biomarkers that are mutated or overexpressed in solid tumors, such as folate receptor-α (FR-α) [12], chlorotoxin [13], epidermal growth factor receptor (EGFR) [14,15] (Fig. 1A), HER2/neu [16] (Fig. 1B), tumor associated antigens (e.g. prostate-specific membrane antigen, PSMA) [17], carcinoembryonic antigen and carbohydrate antigen 19–9 (CA19–9) [18,19]. In addition, aberrant metabolism is also a hallmark of cancer cells, which cultivates a unique tumor metabolic microenvironment with dysregulated extra and intra-cellular pH [20], hypoxia [21] and increased secretion of proteases (e.g. matrix metalloproteinases, cathepsins [22,23] and γ-glutamyltranspeptidase [24]) which are all potential cancer specific targets as well.

Besides the conventional fluorescent imaging method, emerging techniques, such as stimulated Raman scattering (SRS) microscopy [25,26], coherent anti-Stokes Raman scattering (CARS) microscopy [27–30], tetra-hertz radiation imaging [31–33], multiphoton-upconvertion-based imaging [34–36], have also shown great success in pre-clinical animal models. Many of them feature high spatial resolution, fast image acquisition rates, and even label-free *in situ* imaging. Despite their success, these technologies are relatively new and still have technical barriers to overcome before clinical adoption. For example, many Raman microscopy techniques suffer from high background signal and nonlinear dependence of signal intensity versus analyte concentration. Although SRS has overcome many of these concerns, it remains difficult to be translated into clinics in a short time because no SRS

microscope is yet commercially available. In this review, we chose to focus on the fluorescent imaging method and contrast agent development for tumor detection and surgery.

2. Clinical applications for optical imaging

2.1. Anatomical and molecular imaging

Since the dawn of medicine, physicians have wanted to see into the human body to better understand anatomy and how disease can alter it. The discovery of X-rays at the turn of the 20th century provided, for the first time, physicians the ability to see through tissues. The development of CT, enabled by increasing computing power and the digital revolution, improved the sensitivity, tissue resolution and accuracy of imaging by collating large amounts of data from X-rays. This computational revolution intersected with the discovery and development of magnetic resonance as a detectable signal, providing physicians with yet another tool for accurate anatomic imaging. The use of sound waves for SONAR (SOund Navigation And Ranging) during wartime inspired the discovery and use of ultrasound which was able to give real-time anatomic data without exposing the patient to harmful radiation. These modalities provide unprecedented views of the inner workings of the human body and can often be modified to image physiologic parameters as well, such as blood flow with a CT angiogram using iodine contrast. Furthermore, since many solid tumors alter normal anatomy significantly, these imaging techniques are also excellent methods for imaging cancers. With the exception of MRI, however, molecular and physiological information is not readily gleaned except in isolated cases, such as with blood oxygenation level dependent (BOLD) imaging in tumors which can give information on relative hypoxia. Importantly, current imaging modalities are not easily incorporated into the surgical workflow. They are often stand-alone tests conducted in isolation from oncologic surgery. With improved understanding of the genetic underpinnings of cancer, imaging based on the fundamental molecular characteristics of cancer is becoming possible.

FDG-PET is an example of cancer molecular imaging with broad clinical use. Intravenously injected radiolabeled tracers can be detected and reconstructed to generate a three-dimensional image reflecting the tissue distribution of the tracer. FDG is a glucose analog that is actively internalized and retained by metabolically active tissues including cancer cells. FDG-PET imaging is used clinically to image a variety of cancers, including lymphoma, melanoma, head and neck cancer, non-small-cell lung cancer and breast cancer [37–39]. Despite the success of PET imaging in tumor staging and therapeutic assessment, it still comes with a number of disadvantages. Radioactive PET tracers are usually short-lived and PET images have low spatial resolution compared to MRI and CT. While the sensitivity of PET is high, relatively low specificity and false positives are limitations of FDG-PET. One study evaluating FDG-PET surveillance after chemotherapy and radiotherapy for head and neck cancer demonstrated a high negative predictive value of 91.3%, but a relatively low specificity of 81.5% [40]. This is likely due to the FDG accumulation in inflamed tissues from radiation or infection, as well as several metabolically active normal tissues such as brown fat and tonsillar tissue. In addition, since the brain also has high physiologic uptake of glucose and FDG is renally cleared, imaging brain and urologic tumors is difficult.

Optical imaging can be easily coupled with other molecular imaging modalities and image-guided surgery. Many optical imaging techniques rely on fluorescence and bioluminescence as sources of contrast. Compared to MRI, CT and PET, the advantages of optical imaging include lack of ionizing radiation exposure, high spatial resolution, real-time imaging capability, a large field of view, and cameras that are inexpensive and mobile. Benefiting from its long-standing use in cell assays and small animal models, optical imaging offers a wide variety of contrast agents against many different molecular targets. One weakness, the lack of penetration depth due to tissue scattering and absorption of light, prevents its use for whole body imaging. However, for intraoperative guidance, where tumors are often directly visualized, this is a relatively minor disadvantage.

2.2. Contrast-enhanced fluorescent imaging of cancer

The contrast of *in vivo* fluorescent imaging can be improved by increasing the signal through minimizing scattering and absorption by biomolecules, or by reducing the background through avoiding the autofluorescence spectral window. Biological molecules that contain chromophores can absorb photons and transfer the energy into heat, such as hemoglobin, melanin, amino acids that contain aromatic groups (tryptophan, tyrosine and phenylalanine) as well as vitamin derivatives (e.g. retinol, riboflavin and reduced nicotinamide adenine dinucleotide (NADH)). Water, about 70% of human tissue other than fat, also contribute to the extinction spectrum as it shows strong absorption mainly in the infrared region (>1800 nm, excluding a water bending overtone band near 1400–1450 nm [41,42]). In addition to scattering and absorption, endogenous chromophores contribute to autofluorescence [43]. The intensity of autofluorescence is typically orders of magnitude lower than externally introduced fluorophores, but binding or association of these molecules with lipid bilayer membranes or other lipids can enhance their fluorescent quantum yield [44]. The majority of autofluorescence emits between 450 and 650 nm, and disappears beyond ~1500 nm [42,43]. Therefore, the near infrared (NIR) window (650–1700 nm) minimizes photo scattering, absorption and tissue autofluorescence while maximizing tissue penetration.

3. ‘Always-ON’ fluorescent probes for optical tumor imaging

Typical fluorescent labels employ “always ON” modality where fluorescent signal is solely dependent on the probe concentration, relying on accumulation and retention in tumor tissue and clearance of the background probes [45]. To date, several “always ON” probe strategies including small-molecule dyes, biomolecule-dye conjugates and nanoparticles have been evaluated for *in vivo* tumor imaging, image-guided surgery, or both.

3.1. Non-targeted small-molecule dyes

There are two clinically available NIR small molecule dyes, methylene blue and ICG. Methylene blue has been used for macroscopic visualization (dark blue) of ureteral leakage and parathyroid surgery at a high dose (100 mg/kg, intravenous or intra-arterial injection) for decades. One advantage of methylene blue is that it becomes a NIR dye emitting at ~700 nm when sufficiently diluted (0.25–2 mg/kg). Although not clinically approved as a NIR dye, methylene blue has been used successfully to visualize fibrous tumors of the pancreas,

parathyroid adenomas and paragangliomas [46–48] (Fig. 2A). ICG, which emits at ~800 nm, is the only small-molecule NIR fluorescent contrast agent that has been approved for use in surgery. The fact that it is exclusively cleared by the liver, enables its use in assessing the clearance capability of the liver or liver lesions. It has also been used for angiography for many years. A low concentration of ICG has been used off-label for mapping sentinel lymph nodes (SLN), and has shown superiority over blue dyes in terms of penetration depth and sensitivity [49–53] (Fig. 2B). The use of ICG for SLN mapping has paved the road for its application in tumor detection and intraoperative imaging. The mechanism of ICG accumulation in tumors is proposed to be passive targeting resulting from the enhanced permeability and retention (EPR) after binding with plasma proteins [54]. The EPR effect is due to the relatively leaky tumor vasculature and alterations in the structure of lymphatics in cancer. In a pilot study, ICG was used to track microscopic metastasis of ovarian cancers, resulting in the identification of occult disease in areas of normal appearing peritoneum in white light [54]. Ishizawa and colleagues conducted a similar trial aiming to identify small metastatic tumors in patients with hepatocellular carcinoma (HCC) in 2009, and reported a maximal detection depth of 8 mm [55]. Several hours to days after intravenous injection of ICG, a fluorescent rim of the cancerous tissue can be observed during surgery for margin delineation between the surrounding healthy tissue and the tumor. Unfortunately, tumors located deeper than 8 mm were not visualized. Follow-up studies showed that ICG could achieve an almost 100% identification rate for HCC or metastatic colorectal cancer in resected livers [56,57]. ICG has also been used for endoscopic tattooing (a useful technique for labeling and localizing small colorectal lesions) in patients with early colon cancer or colon adenoma and showed 100% accuracy of tumor localization without any adverse effects [58]. Exploiting the EPR effect, many clinical studies have used ICG for detecting other solid tumors, including breast and gastric cancer [59–61]. For example, in breast tumor studies, researchers observed not only a clear and accurate localization and delineation of the tumor but also a slower uptake and outflow rate of ICG in malignant tissues, suggesting the *in vivo* pharmacokinetics of ICG is the significant contributor to ICG's ability to detect cancer [59,62,63].

Another agent, 5-aminolevulinic acid (5-ALA), is the precursor molecule in the porphyrin synthesis pathway, leading to the formation of heme in mammals. It has been clinically approved for cancer diagnosis and cancer photodynamic therapy (PDT) [64]. The last step of heme synthesis is the incorporation of the iron into protoporphyrin IX (PpIX), which requires the activity of ferrochelatases. Excess 5-ALA may cause saturation and exhaustion of limited endogenous ferrochelatases, leading to accumulation of fluorescent PpIX in gliomas, bladder cancer and meningiomas [65–67]. PpIX has two emission peaks with one of them in the NIR window (~705 nm). Since PpIX is also a photosensitizer, 5-ALA can also be introduced as a drug for PDT. The first clinical attempt of using 5-ALA-based PDT was in 1990 [68], and now it has been widely used for the treatment of various malignant neoplasms, including its recent U.S. Food and Drug Administration (FDA) approval of detecting and visualizing malignant tissue in real-time during glioma surgery [69].

Although methylene blue, ICG and 5-ALA have shown selectivity in some clinical studies as discussed above, they are non-targeted small-molecule contrast agents that still exhibit a high background signal. To overcome this limitation, zwitterionic NIR dyes with neutral net

change have been developed with reduced protein binding and fast renal clearance. Data show improved signal over noise ratio compared to conventional NIR fluorophores [70,71]. Despite this, non-targeted small-molecule dyes still suffer from non-specific binding and usually fast clearance reduces the optimal time window for surgery. Moreover, for small molecule agents like 5-ALA, whose signal development is heavily dependent on endogenous enzyme activity, the imaging quality can be highly variable among patients resulting from the lack of a reliable protocol that applies for all patients.

Over the last several decades, many fluorophores in the second NIR window (NIR-II, 950–1700 nm) have been developed and tested in preclinical animal models. By minimizing the background noise from tissue autofluorescence and absorption, they can achieve tissue penetration depths of several centimeters. Dai et al. have reported multiple NIR-II dyes including a synthetic small molecular dye CH1055 that emits at ~1055 nm with a fast clearance through the renal systems within 24 h post-injection [72].

3.2. Biomolecule-dye conjugates

The benefit of targeted imaging design is obvious as the high specificity and affinity between a receptor and its ligand offers a high SNR and potentially a lower dose of the imaging agents. The prolonged circulating time of antibodies may also improve the accumulation of imaging agents in tumors. More importantly, many tumors have been shown to overexpress cell surface receptors which support the proliferation and survival of cancer cells. Consequently, the antibody-dye conjugates have been developed and used in multiple pre-clinical studies.

Epidermal growth factor receptor (EGFR) is frequently overexpressed in many types of cancers, such as glioma, head & neck cancer, liver cancer, lung cancer (squamous cell carcinoma and adenocarcinoma), renal cell carcinoma and ovarian cancer. Overexpression of EGFR is associated with metastasis and poor prognosis [73]. Antibodies against the external domain of EGFR have been developed to target and inhibit EGFR by preventing the binding of its ligands [74]. With the availability of clinically approved monoclonal antibodies against EGFR such as cetuximab and panitumumab, their use as carriers for imaging agents have been extensively studied. Rosenthal et al. showed that Cetuximab-Cy5.5 conjugate intravenously injected into mice bearing head and neck squamous cell carcinoma (HNSCC) tumor xenografts demonstrated higher fluorescence in the tumor than the human skin graft (control group) even 72 h post injection (Fig. 3A–B). Even small tumor (2 mm) metastases demonstrated fluorescence which was confirmed by histopathology [75,76]. They also conducted the first study to use a FDA-approved intraoperative imaging system (SPY™ system, Novadaq, Toronto, Canada) designed for ICG imaging to detect panitumumab-IRDye 800 C W (emission at 795 nm) signals in a preclinical murine model (Fig. 3C–E). The SPY™ system can detect the gross tumor around 1 mm in diameter with a SNR between 1.5 and 3.0 depending on the organs being scanned [77]. These results suggest the feasibility of using fluorescent-labeled antibodies to detect human tumors *in vivo*.

Although antibody-dye conjugates have shown advantages over small-molecule dyes alone, the high production cost and long blood circulation time of humanized antibody raising background signals can be limiting. This has led to use of ligands or small peptides that

preserve the high selectivity and affinity of antibodies with improved pharmacokinetics. Using this approach Grötzinger et al. employed the somatostatin (SST) analog octreotate as a targeting peptide conjugated to indocarbocyanine dyes for imaging a neuroendocrine tumor xenograft model [78]. They observed that the tumor fluorescence increased rapidly within the first 3 h after injection, and was more than 3-fold brighter compared to normal tissue. Ke and colleagues combined EGF with a NIR fluorophore Cy5.5 (emission at 706 nm), which showed a better accumulation within an EGFR-positive breast cancer xenograft tumor than Cy5.5 or ICG alone [79] with almost no detectable fluorescent signal 24 h after injection.

Many other peptide/ligand-dye combinations have been explored in murine models, such as folate-fluorescein isothiocyanate (FITC) [80] and chlorotoxin-Cy5.5 [81]. Folate-FITC that targets folate receptor-α (FR-α) has been tested as an intraoperative fluorescent imaging agent in patients with epithelial ovarian cancer [82]. FR-α is a promising biomarker of ovarian cancer because it is overexpressed in 90%–95% these tumors with low expression in normal tissues. The fluorescence was detectable in all patients with a FR-α-positive malignant tumor. The averaged SNR was 3.1, and the fluorescence could be detected up to 8 h after intravenous injection. Image-guided surgery of a small sized tumor (<1 mm) was feasible. Although the result showcased the potential clinical application of targeted fluorescent imaging in ovarian cancer patients, variable expression levels of FR-α in different tumors and the limitation of FITC in tissue penetration reduce the broad applicability of folate-FITC in a larger series of cancer patients.

Despite the great advances, one major pitfall for targeted agents is expression in normal tissues and the variability of expression in tumor tissues. For example, although EGFR is upregulated in 85% of HNSCC patients, it is also abundant in normal epithelium, especially those adjacent to tumors, making it difficult for accurate margin assessment. Furthermore, it is reported that the EGFR expression level varies from 28 to 3814 fmol per mg of total protein [83] and from 0.3 to 97 according to an immunohistochemistry staining index [84] in head and neck cancer patients. Moreover, not many validated surface biomarkers are shared among a broad range of tumors. For example, FR-α is a good marker for ovarian cancer patients. However, a tissue microarray study from 25 head and neck patients showed no FR-α expression in head and neck cancer cells but only FR-β expression in infiltrating lymphocytes and macrophages [85]. As a result, folate-FITC only showed incomplete delineation of orthotopic head and neck tumors in mice. Overall, this imaging strategy is valuable toward personalized phenotyping of targeted therapy, but may not be as useful in imaging and surgery of a broad range of tumors.

3.3. Nanoparticulate agents

Recently, fluorescent or self-illuminating nanoparticles in the NIR window, such as quantum dots and single-walled carbon nanotubes (SWCN), represent another promising source of fluorophores for tumor detection and image-guided surgery. One advantage of nanoparticle design is that they can potentially incorporate multiple targeting ligands and multichromatic fluorophores, which may yield better targeting efficacy and imaging properties *in vivo* [86]. Quantum dots (QD) are commonly used fluorescent nanoparticles with unique optical

properties, including high photo-stability as well as tunable size-dependent emissions [87]. Compared to conventional organic dyes, QDs are typically brighter and have longer fluorescence lifetime.

In 2004, Gao and colleagues designed core-shell CdSe–ZnS QDs with 650 nm emission wavelength functionalized with polyethylene glycol (PEG) and an antibody to target prostate-specific membrane antigen (PSMA) [88]. The EPR effect as well as the active targeting of human prostate cancer by the antibody contributed to the accumulation and retention of the nanoprobes in tumors. Owing to the unique optical properties of QDs, only 600 pmol QD-PSMA Ab probes was required to illuminate as few as ~1000 cancer cells 2 h post intravenous injection. Although the *in vivo* results were promising, the orange/red-emitting QDs used in this study were not optimized for imaging deeply located tumors. Autofluorescence from the tissue strongly interfered with the signals from QDs requiring a spectral unmixing algorithm to process the original images to extract the QD signal. To address the limitation, the Bawendi group and the Nie group proposed using CdTe/CdSe type-II QDs and alloyed semiconductor QDs that have NIR emission as well as longer lifetime [89,90]. Kim et al. showed that only 400 pmol QDs allowed for sentinel lymph node mapping at 1 cm depth in real-time in the mouse and pig [91].

Rao and coworkers developed a novel CdSe/ZnS QD conjugate that luminesces through bioluminescence resonance energy transfer (BRET) in the absence of external excitation avoiding background autofluorescence [92] using a mutant *Renilla reniformis* luciferase Luc8 with an emission peak at 480 nm to excite the QD655 (fluorescent emission at 655 nm) (Fig. 4A). QD655-Luc8 was able to emit fluorescent and bioluminescent light both *in vitro* and *in vivo* (Fig. 4B, C). Compared with conventional QDs, the self-illuminating QDs greatly enhanced imaging sensitivity by minimizing background fluorescence even at a depth of ~3 mm, showing a remarkable SNR of $>10^3$ for only 5 pmol of QDs. Metal nanoclusters (NCs, e.g. AuNCs and AgNCs) with a size of 2 nm or smaller, also possess unique optical features, such as high quantum yield and stability, low toxicity and bright fluorescence in the visible and NIR range [93–96]. Wu and colleagues have successfully used AuNCs with peak emissions at 710 nm for tumor imaging of breast and cervical cancer xenografts in mice with a high SNR of 15 [97].

Compared with the conventional NIR imaging, fluorescent imaging in the NIR-II window has emerged only in recent years, owing to lack of suitable biocompatible molecules and long-wavelength cameras. Actually, many nanomaterials, such as SWCNs, have intrinsic fluorescent emission in the NIR-II window. In 2009, Welsher et al. reported the first *in vivo* NIR-II fluorescent imaging of mice tumor vasculatures using PEG-lyated SWCNs and a long-wavelength indium–gallium–arsenide (InGaAs) camera that was capable of doing fluorescence imaging in the range of 1000–1700 nm [98]. The same group further functionalized SWCNs with poly(maleic anhydride-*alt*-1-octadecene)-poly(ethylene glycol) methyl ether (C_{18}-PMH-mPEG), and achieved 30% injected dose (ID) per gram of tumor accumulation in 4T1 murine breast tumors in Balb/c mice with only 3.6 mg/kg ID [99,100]. Tumor fluorescence could be observed as early as 6 h post-injection. A high contrast image was observed after 1 day when most SWCNs were cleared from the blood. Moreover, very low autofluorescence was observed in the 1.1–1.7 mm detection range.

Overall, the tunable size and ease of surface modification of inorganic nanoparticles may make them advantageous over conventional organic dyes and biomolecule-dye conjugates. However, these imaging probes are also ‘always-ON’ agents, whose contrast relies on their accumulation and retention in cancerous tissues. Also, accumulation of heavy metals and non-degradable nanomaterials, such as QDs and carbon nanotubes, poses safety concerns for clinical use. Although the EPR effect and active targeting strategies improve accumulation, prolonged circulation of unbound molecules can still lead to false positives or high background fluorescence. Small-molecule dyes are rapidly cleared, partially addressing this problem, however, the absolute amount that can be delivered to the tumor is decreased by the increased rate of excretion. Clearance of small molecular agents from tumor site further limits the time window for surgical applications. Because of these limitations, a ‘smart’ imaging probe design that stays silent in the normal tissue background and only turns on at tumor sites and stays on after activation could resolve the dilemma of ‘always ON’ probes.

4. Stimuli-responsive nanoprobes for tumor detection and image-guided surgery

Most activatable fluorophores display marked changes in optical properties, such as emission wavelengths or fluorescent intensities, upon interacting with tumor specific signals. Several photochemical processes are typically used in the design of activatable probes. Fluorescence resonance energy transfer (FRET) is a classical strategy that can be used to change the wavelength of the emitting light (hetero-FRET) or the intensity of the fluorescence (homo-FRET). An example of a hetero-FRET nanoparticle is a fluorescent semi-conductive polymer that absorbs light at 400–600 nm (FRET donor) and a NIR small molecule dye NIR775 (FRET acceptor). When excited at 465 nm, a persistent luminescent signal at 775 nm could be observed for 1 h, allowing live animal imaging [101]. An example of homo-FRET imaging agents is ICG, which tends to form dimers or trimers in aqueous solution, leading to a homo-FRET-based fluorescence self-quenching. Nakajima et al. synthesized a monoclonal antibody against PSMA conjugated with multiple copies of ICG, resulting in a fluorescent signal quenching. After internalization into tumor cells through PSMA binding, an 18-fold activation of signal was observed up to 10 days due to separation of the ICG molecules [102]. Another strategy of fluorescence quenching is photon-induced electron transfer (PeT). Similar to FRET, the electrons transferred from a PeT donor can diminish the fluorescence emission of the excited fluorophores. Therefore, when the PeT donor is deactivated from the fluorophore, full activation of the fluorescent signal can be achieved. This strategy is usually for designing small-molecule fluorophores that rely on environmental cues, such as pH, ROS, metal ions, and enzymes, to cleave the PeT donor [103].

4.1. Enzyme-activatable probes

Enzymatic activation of imaging probes by proteases such as matrix metalloproteases (MMP), lysosomal hydrolases and cathepsins has been used as a strategy to activate probes specifically in tumors. MMPs are found in the extracellular environment in pathologic conditions such as inflammation, but are also commonly overexpressed in cancer cells and secreted into the tumor micro-environment, and contribute to extracellular matrix (ECM)

remodeling and cancer metastasis. Intracellular lysosomal hydrolases in cancer cells can also be used for signal activation after cancer cell surface targeting and internalization.

In 1999, Weissleder and colleagues first developed a copolymer consisting of poly-$_L$-lysine and methoxypolyethylene glycol succinate conjugated with Cy5.5 [22] (Fig. 5A). The fluorescence was self-quenched before enzyme activation (Fig. 5A–C). Afterwards, 95% of the quenched fluorescence was recovered when the nanoparticle was internalized into cancer cells, resulting in a 12-fold increase in the fluorescent signal. Tumors as small as 300 μm were detected 24 h after injection of the probe (Fig. 5D–I). In addition to tumor imaging, this design also offers additional molecular information such as cathepsin activity in the tumors. One disadvantage of enzyme-based strategies is the long time to full activation, which can sometimes take days. To address this weakness, Urano et al. designed a pro-dye substrate of γ-glutamyltranspeptidase (GGT), a cell-surface-bound enzyme overexpressed in cervical and ovarian cancers. The pro-dye, γ-glutamyl-hydroxymethyl rhodamine green (gGlu-HMRG), is activated within 1 min after topical application in a murine ovarian cancer model, with fluorescence lasting for at least an hour [104]. Topical administration also reduced the required dose compared to systemic injection. The fluorescence of gGlu-HMRG was quenched at neutral pH because of the preferred spirocyclization state; however, it became highly fluorescent after the cleavage of the gGlu group by GGT on tumor cell surface. A similar design sensitive to β-galactosidase was developed by the same group [105]. Although enzyme-activatable imaging agents achieved success in mouse xenograft models, the highly variable activity and expression level of the enzymes in patients, which is critical for determining the optimal surgery time window, may hamper their clinical implementation.

4.2. pH-sensitive probes

In 1924, Otto Warburg observed that cancer cells generally have a higher rate of glycolysis followed by lactic acid fermentation compared to the oxidation of pyruvate in normal cells. This metabolic difference persists even in normoxia causing accumulation of lactic acid in the tumor microenvironment. Also, many carboxylate transporters are overexpressed on the cancer cell surface, facilitating the export of excessive protons from the cytoplasm. In line with Warburg's theory, Voegtlin and Kahler, for the first time, reported extracellular tumor acidosis in Rous chicken sarcoma in 1932 [106]. To target this metabolic difference between normal and cancer cells, many pH-responsive probes have been designed for tumor detection and image-guided surgery. An ideal pH-sensitive imaging probe should (i) be almost nonfluorescent in the blood or interstitial fluid surrounding normal tissues, i.e. pH 7.4; (ii) be highly fluorescent in acidic environment, e.g. tumor microenvironment (pH < 6.9) and endocytic organelles (pH < 6); (iii) emit NIR light to improve signal over noise for *in vivo* imaging.

4.2.1. Small molecular pH sensors—To achieve pH response in small-molecule dyes, PeT is a commonly used strategy. The PeT donor quenches the fluorescence of a small-molecule dye at neutral pH; protonation of the PeT donor blocks the energy transfer leading to fluorescence recovery. The Kobayashi group has developed a series of pH-sensitive probes using different anilines as the proton-sensitive group and 2,6-dicarboxyethyl-1,3,5,7-

tetramethyl-boron-dipyrromethene (BODIPY, emission > 500 nm) as the fluorescent dye [107]. The carboxylic groups allowed the conjugation of the molecules to a human epidermal growth factor receptor type 2 (HER2) targeting antibody trastuzumab. By using different anilines with different pK_a values, they synthesized multiple probes responsive to pH changes from 3.8 to 6.0. As a result, they could be activated in the low-pH environment of lysosomes after internalization through binding with HER2. The probe with a pK_a at 6.0 showed a 22-fold higher SNR comparing with a pH-insensitive probe *in vivo* with a tumor-detection specificity of 99.1%. Xiong et al. used a similar strategy while substituting the antibodies with PEG chains, achieving a tumor-to-liver ratio of 3 when a probe with a pK_a of 4.5 was injected [108]. Despite aforementioned success in animal models, the pH response range of small-molecule pH sensors can be too broad (~2 pH for a 10-fold fluorescent signal increase) to accurately differentiate the tumor microenvironment (pH 6.7–7.0) from blood (pH 7.4).

4.2.2. Targeted pH sensitive agents—The decoration of pH-sensitive dyes with tumor specific ligands is an effective strategy to enhance tumor specificity of the probe. For example, Lee and colleagues conjugated pH-sensitive Cy5 dye to a cyclic arginine-glycine-aspartic acid (cRGD) peptide targeting αvβ3 integrin, a protein that is highly overexpressed in endothelial cells during tumor angiogenesis [109] to successfully image tumors. Another strategy is to exploit the conformational change of proteins and peptides upon protonation. The pH low-insertion peptide (pHLIP™) represents such a system [110] (Fig. 6A, B). The peptide has a pK_a around 6, and is water-soluble at higher pH (e.g. pH = 8, state I). At lower pH, it collapses on the surface of the lipid bi-layer membrane and remains as an unstructured monomer (state II). The protonation of the Asp residues enhances the hydrophobicity of the peptide, leading to the formation of a transmembrane α-helix structure (folding and insertion, state III) (Fig. 6A). The fluorescence of the two tryptophan residues on the peptide reports the change of the peptide from membrane attachment to membrane insertion. The system represents a useful tool to target cells in a milieu with elevated levels of extracellular acidity, such as cancer and inflammation. Furthermore, the termini of the peptide can be functionalized with fluorescent dyes or other molecules for cytosolic delivery. When a NIR dye, such as Cy 5.5 or Alexa 750, is attached to the N-terminus of pHLIP™, tumors that were 2–4 mm in diameter were successfully imaged. The pHLIP™ system was used to demonstrate that co-injection with glucose decreases extracellular pH of tumors by at least 0.3 pH units, and increases tumor targeting in a dose-dependent manner due to increased metabolic activity. In contrast, giving animals bicarbonate water, which increases tissue pH, correlated with a decreased tumor fluorescence. More aggressive metastatic tumors are thought to have a lower extracelluar pH because extracellular acidity promotes the activity of proteases and metastasis. In a mouse model of both metastatic (M4A4) and non-metastatic (NM2C5) tumors, the fluorescent signals from Alexa750-pHLIP™ was 1.5–1.6 times higher in M4A4 tumors with a pH of 6.9 ± 0.2 compared with 7.1 ± 0.2 in the less aggressive NM2C5 tumors [111] (Fig. 6 C–F).

Despite the success in mouse xenograft models, the relatively low SNR (2–5), high false positive signals in the kidney and long activation time (48–72 h) [111] may limit the clinical translation of pHLIP™. Recently, some pHLIP™ variants have been developed to fine tune

the tumor-targeting efficiency and to achieve a rapid background signal reduction [112]. Although the optimal SNR can be achieved within 24 h, these variants still have broad pH response spanning ~2 pH units limiting signal amplification of pH differences between tumor and normal tissues.

4.2.3. Polymer-based ultra pH-sensitive probes—Polymer nanomaterials have been developed as stimuli-responsive nanoprobes for tumor detection and image-guided surgery. Typical pH-sensitive groups consist of tertiary amines, carboxylic acids and sulfonamides that exhibit distinct protonation and de-protonation states. Introduction of acid-liable covalent linkages is another commonly used strategy.

Recently, a series of tunable ultra pH-sensitive (UPS) nanoprobes have been developed for broad biomedical imaging applications, including quantitative endo/lysosomal imaging, tumor detection and image-guided surgery [113–117]. They fluoresce upon contact with a very narrow pH range (<0.25 pH units), which allows for a threshold response to subtle pH changes. The building blocks of UPS nanoprobes are a series of block copolymers (PEO-*b*-PR, where PEO is poly (ethylene oxide) and PR is the ionizable block with precisely controlled hydrophobic segments). When PR reaches a critical threshold of hydrophobicity, micellization/nanophase transition drives a cooperative deprotonation of charged polymers, rendering a fast and ultrasensitive pH response with micelle formation in aqueous solution. Conjugation of fluorescent dyes on the PR segment quenches fluorescence at higher pH due to homo-FRET effect. A drop below the transition pH leads to a sharp and exponential increase of fluorescent intensity due to micelle dissociation into the individual polymer components and dequenching of the attached dye. Many previously reported pH-sensitive nanosystems do not have such a sharp response in the physiological pH range and sometimes take a long time (e.g. 24 h) to respond. In contrast, the proton transfer and non-covalent self-assembly in the UPS system renders a fast (<5 ms), sharp and tunable response [118].

To visualize tumors *in vivo*, a UPS nanoprobe with a transition pH at 6.9 and encoded with ICG (ICG-UPS) was employed to distinguish the small pH difference between blood (7.4) and the acidic extracellular pH (pH_e) of tumors (6.5–6.8) [114] (Fig. 7A). The resulting nanosensor was not only able to detect a broad range of tumors in mouse models, but also to enable real-time image-guided resection of established tumors and occult nodules [20]. By using a clinical SPY™ Elite camera, ICG-UPS can achieve high tumor over normal tissue ratio (>20) in a wide variety of tumor models (Fig. 7B) compared to ICG-loaded PEG-*b*-poly(lactic acid) and free ICG. Qualitative comparisons with FDG-PET showed that ICG-UPS could pick up small tumor nodules (~10 mm^3) and delineate tumor with greater sensitivity and specificity. In a real-time image-guided tumor resection in mice, ICG-UPS achieved 100% calculated sensitivity and specificity (95% confidence interval, 72–100%, Fig. 7C), and showed improved overall survival rate (72% animals cured 150 days post-surgery) compared with white light surgery, debulking surgery and untreated controls (Fig. 7D).

4.3. ROS- and hypoxia-responsive nanomaterials

Although tumor angiogenesis is a hallmark of cancer, sometimes the newly formed vessels cannot meet the metabolic demands of the cancer cells, leading to a relatively hypoxic tumor microenvironment with many stress factors, like reactive oxygen species (ROS). Hypoxia and ROS are examples of tumor specific metabolic changes that can be exploited for imaging. Many fluorescent proteins (e.g. cpYFP [119], HyPer [120] and roGFP1 [121]) and small molecules (e.g. dichlorodihydrofluorescein [122], aryl boronates- or α-ketoacid-containing molecules [123]) have been developed for detecting intracellular ROS, but none are suitable for *in vivo* tumor detection because of limited tissue penetration depth. Murthy et al. reported the first imaging agent targeting ROS levels, especially hydrogen peroxide levels, in animals in 2007 [124]. The probe design was based on a three-component chemiluminescent reaction between the peroxalate polymers, the fluorescent dye pentacene and hydrogen peroxide. The peroxalate ester group generated high-energy dioxetanedione, which reacted with hydrogen peroxide to excite polymer encapsulated fluorescent dyes. One advantage of the peroxalate nanoprobe is that dioxetanedione can chemically excite a wide variety of fluorescent dyes, including NIR dyes (e.g. pentacene, emission ~630 nm). Recently, Pu and colleagues developed the an NIR ratiometric photoacoustic nanoprobe that was capable of real-time imaging of ROS *in vivo* [125]. The nanoprobe is composed of two semiconducting polymers (SP) with strong absorption in the NIR region and a ROS-sensitive cyanine dye derivative (IR775S). When excited at 700 nm and 820 nm, the SP nanoprobe and IR775S gave distinct photoacoustic peaks. In the presence of ROS, the signal from IR775S was largely diminished but SP nanoprobe stayed unchanged. Therefore, the signal ratio between 700 nm and 820 nm can be used as a ratiometric tool to quantify ROS levels *in vivo*. Although neither nanoprobe was studied in tumor models, given the role that ROS plays in tumor pathogenesis and progression, these nanoprobes represent a promising source of imaging agents that possess translational potential in tumor imaging.

Conventional hypoxia imaging probes are based on nitroimidazole compounds that are often used in PET and MRI studies. Recently, Zheng and colleagues synthesized a poly(N-vinylpyrrolidone) (PVP)-conjugated iridium (III) complex probe sensitive to oxygen levels with emitted fluorescence in the NIR region [21]. A small decrease of the oxygen level led to a sharp increase in the phosphorescent intensity of the probe. In this Ir-PVP nanoprobe, the phosphorescence of iridium (III) was quenched in the normal tissues, but was turned on in cancerous regions with lower oxygen levels. The hydrophilic PVP segment improved bio-distribution and the pharmacokinetic profile for improved tumor imaging. The Ir-PVP probe showed minimal background signal in normal tissues, and could detect small metastatic tumors and as few as 10^3 cancer cells *in vivo* up to 9 mm in depth. Table 1.

5. Summary and future outlook

Anatomical and molecular imaging techniques have unique advantages and limitations for tumor detection and image-guided surgery as described above. Among these modalities, fluorescent molecular imaging offers a safe, real-time and non-invasive approach, which can delineate tumor margins and disclose cellular and molecular functional information in solid cancers.

Compared with conventional optical imaging in the visible spectrum, NIR fluorescent imaging has demonstrated superior resolution and tissue penetration, as well as much lower background signals from either ambient light and/or tissue autofluorescence, which is critical for image-guided surgery in the OR. For example, although both ICG and 5-ALA are clinically approved optical imaging agents, surgeons still need to turn off the room light to visualize the signal of 5-ALA induced PpIX fluorescence due to its shorter emission wavelength, which is a major disruption of the surgical workflow [135]. In contrast, the emission spectrum of ICG falls in NIR-I window, which stands out from the relatively low ambient NIR background signals. However, the availability of FDA-approved NIR probes is still limited. Although new NIR-I and NIR-II probes are emerging, many of them still suffer from high hydrophobicity (e.g. carbon nanotubes) and low quantum yield (e.g. CH1005 only has a quantum yield of 0.3%). Hence, image-guided surgery calls for more FDA-approved NIR probes with good biocompatibility and high quantum yield. Recently, Antaris et al. tailored CH1005 by changing the functional end groups from carboxylic to sulfonic acid, which dramatically improved its aqueous solubility. Moreover, new NIR-II dye CH-4T readily formed supramolecular complex with plasma proteins, resulting in ~110-fold increase in fluorescence intensity and ~25-fold decrease in dose, which could potentially be adopted for image-guided surgery with good safety profile, fast imaging speed and deep tissue penetration [136].

Although there is a large unmet need for new NIR probes, high development costs and regulatory hurdles hamper development. On the other hand, integrating clinically approved therapeutic antibodies with existing hydrophilic NIR dyes offers a logical and promising approach for shortening the development of new cancer-specific imaging agents. Multiple targeted optical probes are under evaluation for tumor detection in clinical trials, such as folate-NIR dye for ovarian cancer surgery and cetuximab-IRDye800 C W for resection of head and neck squamous cell carcinoma. However, this approach may be limited by the lack of broad cancer detection capability across diverse cancer phenotypes as well as inter- and intra-tumoral variability of target expressions over normal tissues. In addition, the always-ON design may elevate background signals that hamper the accurate detection of tumor-specific signals. Development of new nanoparticle probes with stimuli-responsive properties to turn on the optical probes from a silent state in normal physiology to an illuminating state in tumors offers a useful strategy to improve the sensitivity and specificity of tumor detection. Unlike small molecular designs, the cooperative behaviors of nanosystems, which are rooted in supramolecular self-assembly, can be exploited for the development of transistor-like nanosensors to amplify pathological signals to further improve the accuracy of tumor detection [118]. Many cancer-specific biomarkers have been largely explored for designing stimuli-responsive nanoprobes, including acidic tumor microenvironment, high ROS and/or hypoxia and overexpressed proteolytic enzymes or angiogenesis/invasion markers. However, they all have their own limitations in terms of clinical adoption. For example, although hypoxia represents a hallmark of cancer, it is most profound in the center of a tumor, which may be less accessible for most nanoprobes and also result in dim fluorescent signals and represents the area of the cancer least relevant to surgical margins. While many types of cancer show elevated levels of ROS and proteolytic enzymes that are secreted to promote metastasis, the numbers vary greatly among patients and/or different

cancer types, which may result in inter- and intra-tumoral variation when converted into fluorescent signals. Acidic pH around tumor margins offers a promising and robust biomarker that can be utilized by fluorescent tumor imaging probes, but preclinical pH-responsive probes are still facing ‘translational gaps’ including safety assessment and clinical validations. Thus, the in-depth multidisciplinary collaboration among scientists, engineers and surgeons is required to accelerate the development and translation of fluorescent imaging probes for cancer surgery.

Acknowledgement

This work was supported by the grant from the National Institutes of Health (R01CA192221 and R01CA211930 to J.G. and B.D.S.). C.W. was a Howard Hughes Medical Institute (HHMI) International Student Research Fellow. Fig. 1 is based on data generated by the TCGA Research Network: http://cancergenome.nih.gov/.

References

[1]. N.C. Institute, Cancer stat fact sheets, 2016 http://seer.cancer.gov/statfacts/.

[2]. Sudhakar A, History of Cancer, ancient and modern treatment methods, J. Cancer Sci. Ther 1 (2) (2009) 1–4. [PubMed: 20740081]

[3]. Ding D, Kwok RT, Yuan Y, Feng G, Tang BZ, Liu B, A fluorescent light-up nanoparticle probe with aggregation-induced emission characteristics and tumor-acidity responsiveness for targeted imaging and selective suppression of cancer cells, Mater. Horizons 2 (1) (2015) 100–105.

[4]. Kubben PL, ter Meulen KJ, Schijns OE, ter Laak-Poort MP, van Overbeeke JJ, van Santbrink H, Intraoperative MRI-guided resection of glioblastoma multiforme: a systematic review, Lancet Oncol 12 (11) (2011) 1062–1070. [PubMed: 21868286]

[5]. Vahrmeijer AL, Hutteman M, van der Vorst JR, van de Velde CJ, Frangioni JV, Image-guided cancer surgery using near-infrared fluorescence, Nature reviews, Clin. Oncol 10 (9) (2013) 507–518.

[6]. Nguyen QT, Tsien RY, Fluorescence-guided surgery with live molecular navigation–a new cutting edge, Nat. Rev. Cancer 13 (9) (2013) 653–662. [PubMed: 23924645]

[7]. Dacosta RS, Wilson BC, Marcon NE, Spectroscopy and fluorescence in esophageal diseases, Best. Pract. Res. Clin. Gastroenterol 20 (1) (2006) 41–57. [PubMed: 16473800]

[8]. Draga RO, Grimbergen MC, Vijverberg PL, van Swol CF, Jonges TG, Kummer JL Bosch Ruud, In vivo bladder cancer diagnosis by high volume Raman spectroscopy, Anal. Chem 82 (14) (2010) 5993–5999. [PubMed: 20524627]

[9]. Haka AS, Volynskaya Z, Gardecki JA, Nazemi J, Lyons J, Hicks D, Fitzmaurice M, Dasari RR, Crowe JP, Feld MS, In vivo margin assessment during partial mastectomy breast surgery using raman spectroscopy, Cancer Res 66 (6) (2006) 3317–3322. [PubMed: 16540686]

[10]. Schwarz RA, Gao W, Redden Weber C, Kurachi C, Lee JJ, El-Naggar AK, Richards-Kortum R, Gillenwater AM, Noninvasive evaluation of oral lesions using depth-sensitive optical spectroscopy, Cancer 115 (8) (2009) 1669–1679. [PubMed: 19170229]

[11]. Mo J, Zheng W, Low JJ, Ng J, Ilancheran A, Huang Z, High wavenumber Raman spectroscopy for in vivo detection of cervical dysplasia, Anal. Chem 81 (21) (2009) 8908–8915. [PubMed: 19817391]

[12]. van Dam GM, Themelis G, Crane LM, Harlaar NJ, Pleijhuis RG, Kelder W, Sarantopoulos A, de Jong JS, Arts HJ, van der Zee AG, Bart J, Low PS, Ntziachristos V, Intraoperative tumor-specific fluorescence imaging in ovarian cancer by folate receptor-alpha targeting: first in-human results, Nat. Med 17 (10) (2011) 1315–1319. [PubMed: 21926976]

[13]. Veiseh M, Gabikian P, Bahrami SB, Veiseh O, Zhang M, Hackman RC, Ravanpay AC, Stroud MR, Kusuma Y, Hansen SJ, Kwok D, Munoz NM, Sze RW, Grady WM, Greenberg NM, Ellenbogen RG, Olson JM, Tumor paint: a chlorotoxin:Cy5.5 bioconjugate for intraoperative visualization of cancer foci, Cancer Res 67 (14) (2007) 6882–6888. [PubMed: 17638899]

[14]. Ke S, Wen X, Gurfinkel M, Charnsangavej C, Wallace S, Sevick-Muraca EM, Li C, Near-infrared optical imaging of epidermal growth factor receptor in breast cancer xenografts, Cancer Res 63 (22) (2003) 7870–7875. [PubMed: 14633715]

[15]. Urano Y, Asanuma D, Hama Y, Koyama Y, Barrett T, Kamiya M, Nagano T, Watanabe T, Hasegawa A, Choyke PL, Kobayashi H, Selective molecular imaging of viable cancer cells with pH-activatable fluorescence probes, Nat. Med 15 (1) (2009) 104–109. [PubMed: 19029979]

[16]. Koyama Y, Hama Y, Urano Y, Nguyen DM, Choyke PL, Kobayashi H, Spectral fluorescence molecular imaging of lung metastases targeting HER2/ neu, Clin. Cancer Res 13 (10) (2007) 2936–2945. [PubMed: 17504994]

[17]. Nakajima T, Mitsunaga M, Bander NH, Heston WD, Choyke PL, Kobayashi H, Targeted, activatable, in vivo fluorescence imaging of prostate-specific membrane antigen (PSMA) positive tumors using the quenched humanized J591 antibody-indocyanine green (ICG) conjugate, Bioconjug. Chem 22 (8) (2011) 1700–1705. [PubMed: 21740058]

[18]. Tran Cao HS, Kaushal S, Metildi CA, Menen RS, Lee C, Snyder CS, Messer K, Pu M, Luiken GA, Talamini MA, Hoffman RM, Bouvet M, Tumor-specific fluorescence antibody imaging enables accurate staging laparoscopy in an orthotopic model of pancreatic cancer, Hepatogastroenterology 59 (118) (2012) 1994–1999. [PubMed: 22369743]

[19]. McElroy M, Kaushal S, Luiken GA, Talamini MA, Moossa AR, Hoffman RM, Bouvet M, Imaging of primary and metastatic pancreatic cancer using a fluorophore-conjugated anti-CA19–9 antibody for surgical navigation, World J. Surg 32 (6) (2008) 1057–1066. [PubMed: 18264829]

[20]. Zhao T, Huang G, Li Y, Yang S, Ramezani S, Lin Z, Wang Y, Ma X, Zeng Z, Luo M, A transistor-like pH nanoprobe for tumour detection and image-guided surgery, Nat. Biomed. Eng 1 (2016) 0006. [PubMed: 28966871]

[21]. Zheng X, Wang X, Mao H, Wu W, Liu B, Jiang X, Hypoxia-specific ultrasensitive detection of tumours and cancer cells in vivo, Nat. Comm 6 (2015).

[22]. Weissleder R, Tung C-H, Mahmood U, Bogdanov A, In vivo imaging of tumors with protease-activated near-infrared fluorescent probes, Nat. Biotechnol 17 (4) (1999) 375–378. [PubMed: 10207887]

[23]. Tung C-H, Mahmood U, Bredow S, Weissleder R, In vivo imaging of proteolytic enzyme activity using a novel molecular reporter, Cancer Res 60 (17) (2000) 4953–4958. [PubMed: 10987312]

[24]. Urano Y, Sakabe M, Kosaka N, Ogawa M, Mitsunaga M, Asanuma D, Kamiya M, Young MR, Nagano T, Choyke PL, Rapid cancer detection by topically spraying a γ-glutamyltranspeptidase–activated fluorescent probe, Sci. Transl. Med 3 (110) (2011), 110ra119.

[25]. Ji M, Lewis S, Camelo-Piragua S, Ramkissoon SH, Snuderl M, Venneti S, Fisher-Hubbard A, Garrard M, Fu D, Wang AC, Detection of human brain tumor infiltration with quantitative stimulated Raman scattering microscopy, Sci. Transl. Med 7 (309) (2015), 309ra163–309ra163.

[26]. Freudiger CW, Min W, Saar BG, Lu S, Holtom GR, He C, Tsai JC, Kang JX, Xie XS, Label-free biomedical imaging with high sensitivity by stimulated Raman scattering microscopy, Sci 322 (5909) (2008) 1857–1861.

[27]. Zumbusch A, Holtom GR, Xie XS, Three-dimensional vibrational imaging by coherent anti-Stokes Raman scattering, Phys. Rev. Lett 82 (20) (1999) 4142.

[28]. Ichimura T, Hayazawa N, Hashimoto M, Inouye Y, Kawata S, Tip-enhanced coherent anti-Stokes Raman scattering for vibrational nanoimaging, Phys. Rev. Lett 92 (22) (2004), 220801. [PubMed: 15245207]

[29]. Uckermann O, Galli R, Tamosaityte S, Leipnitz E, Geiger KD, Schackert G, Koch E, Steiner G, Kirsch M, Label-free delineation of brain tumors by coherent anti-stokes Raman scattering microscopy in an orthotopic mouse model and human glioblastoma, PLoS One 9 (9) (2014), e107115. [PubMed: 25198698]

[30]. Evans CL, Potma EO, Puoris' haag M, Côté D, Lin CP, Xie XS, Chemical imaging of tissue in vivo with video-rate coherent anti-Stokes Raman scattering microscopy, Proc. Natl. Acad. Sci. U. S. A 102 (46) (2005) 16807–16812. [PubMed: 16263923]

[31]. Siegel PH, Terahertz technology in biology and medicine, IEEE Trans. Microw. Theory Techn 52 (10) (2004) 2438–2447.

[32]. Chen H, Chen T-H, Tseng T-F, Lu J-T, Kuo C-C, Fu S-C, Lee W-J, Tsai Y-F, Huang Y-Y, Chuang EY, High-sensitivity in vivo THz transmission imaging of early human breast cancer in a subcutaneous xenograft mouse model, Opt. express 19 (22) (2011) 21552–21562. [PubMed: 22109004]

[33]. Yang X, Zhao X, Yang K, Liu Y, Liu Y, Fu W, Luo Y, Biomedical applications of terahertz spectroscopy and imaging, Trends Biotechnol 34 (10) (2016) 810–824. [PubMed: 27207226]

[34]. Xiong L, Chen Z, Tian Q, Cao T, Xu C, Li F, High contrast upconversion luminescence targeted imaging in vivo using peptide-labeled nanophosphors, Anal. Chem 81 (21) (2009) 8687–8694. [PubMed: 19817386]

[35]. Chen Q, Wang C, Cheng L, He W, Cheng Z, Liu Z, Protein modified upconversion nanoparticles for imaging-guided combined photothermal and photodynamic therapy, Biomaterials 35 (9) (2014) 2915–2923. [PubMed: 24412081]

[36]. Zhou J, Liu Z, Li F, Upconversion nanophosphors for small-animal imaging, Chem. Soc. Rev 41 (3) (2012) 1323–1349. [PubMed: 22008740]

[37]. Gambhir SS, Molecular imaging of cancer with positron emission tomography, Nat. Rev. Cancer 2 (9) (2002) 683–693. [PubMed: 12209157]

[38]. Quon A, Gambhir SS, FDG-PET and beyond: molecular breast cancer imaging, J. Clin. Oncol 23 (8) (2005) 1664–1673. [PubMed: 15755974]

[39]. Juweid ME, Cheson BD, Positron-emission tomography and assessment of cancer therapy, N. Engl. J. Med 354 (5) (2006) 496–507. [PubMed: 16452561]

[40]. Kubota K, Yokoyama J, Yamaguchi K, Ono S, Qureshy A, Itoh M, Fukuda H, FDG-PET delayed imaging the detection of head and neck cancer recurrence after radio-chemotherapy comparison with MRI/CT, Eur. J. Nucl. Med. Mol. Imaging 31 (4) (2004) 590–595. [PubMed: 14722678]

[41]. Büning-Pfaue H, Analysis of water in food by near infrared spectroscopy, Food Chem 82 (1) (2003) 107–115.

[42]. Hong G, Antaris AL, Dai H, Near-infrared fluorophores for biomedical imaging, Nat. Biomed. Eng 1 (2017) 0010.

[43]. Zipfel WR, Williams RM, Christie R, Nikitin AY, Hyman BT, Webb WW, Live tissue intrinsic emission microscopy using multiphoton-excited native fluorescence and second harmonic generation, Proc. Natl. Acad. Sci. U. S. A 100 (12) (2003) 7075–7080. [PubMed: 12756303]

[44]. Xu C, Zipfel W, Shear JB, Williams RM, Webb WW, Multiphoton fluorescence excitation: new spectral windows for biological nonlinear microscopy, Proc. Natl. Acad. Sci. U. S. A 93 (20) (1996) 10763–10768. [PubMed: 8855254]

[45]. Wang Z, Luo M, Mao C, Wei Q, Zhao T, Li Y, Huang G, Gao J, A redoxactivatable fluorescent sensor for the high-throughput quantification of cytosolic delivery of macromolecules, Angew. Chem 129 (5) (2017) 1339–1343.

[46]. van der Vorst JR, Vahrmeijer AL, Hutteman M, Bosse T, Smit VT, van de Velde C, Frangioni JV, Bonsing BA, Near-infrared fluorescence imaging of a solitary fibrous tumor of the pancreas using methylene blue, World J. Gastrointest. Surg 4 (7) (2012) 180–184. [PubMed: 22905287]

[47]. Tummers QR, Boonstra MC, Frangioni JV, van de Velde CJ, Vahrmeijer AL, Bonsing BA, Intraoperative near-infrared fluorescence imaging of a paraganglioma using methylene blue: a case report, Int. J. Surg. Case Rep 6 (2015) 150–153.

[48]. Vorst JR, Schaafsma BE, Verbeek FP, Swijnenburg RJ, Tummers QR, Hutteman M, Hamming JF, Kievit J, Frangioni JV, Velde CJ, Intraoperative near-infrared fluorescence imaging of parathyroid adenomas with use of low-dose methylene blue, Head neck 36 (6) (2014) 853–858. [PubMed: 23720199]

[49]. Gioux S, Choi HS, Frangioni JV, Image-guided surgery using invisible near-infrared light: fundamentals of clinical translation, Mol. Imaging 9 (5) (2010) 7290, 2010. 00034.

[50]. Mieog JSD, Troyan SL, Hutteman M, Donohoe KJ, van der Vorst JR, Stockdale A, Liefers G-J, Choi HS, Gibbs-Strauss SL, Putter H, Toward optimization of imaging system and lymphatic tracer for near-infrared fluorescent sentinel lymph node mapping in breast cancer, Ann. Surg. Oncol 18 (9) (2011) 2483–2491. [PubMed: 21360250]

[51]. Schaafsma BE, Mieog JSD, Hutteman M, Van der Vorst JR, Kuppen PJ, Löwik CW, Frangioni JV, Van de Velde CJ, Vahrmeijer AL, The clinical use of indocyanine green as a near-infrared

fluorescent contrast agent for image-guided oncologic surgery, J. Surg. Oncol 104 (3) (2011) 323–332. [PubMed: 21495033]

[52]. Sevick-Muraca EM, Sharma R, Rasmussen JC, Marshall MV, Wendt JA, Pham HQ, Bonefas E, Houston JP, Sampath L, Adams KE, Imaging of lymph flow in breast cancer patients after microdose administration of a near-infrared fluorophore Feasibility study 1, Radiology 246 (3) (2008) 734–741. [PubMed: 18223125]

[53]. Hutteman M, Mieog JSD, van der Vorst JR, Liefers GJ, Putter H, Löwik CW, Frangioni JV, van de Velde CJ, Vahrmeijer AL, Randomized, double-blind comparison of indocyanine green with or without albumin premixing for near-infrared fluorescence imaging of sentinel lymph nodes in breast cancer patients, Breast Cancer Res. Treat 127 (1) (2011) 163–170. [PubMed: 21360075]

[54]. Horowitz N, Penson R, Kassis E, Foster R, Seiden M, Weissleder R, Fuller A, Laparoscopy in the near infrared with ICG detects microscopic tumor in women with ovarian cancer: 0078, Int. J. Gynecol. Cancer 16 (2006) 622.

[55]. Ishizawa T, Fukushima N, Shibahara J, Masuda K, Tamura S, Aoki T, Hasegawa K, Beck Y, Fukayama M, Kokudo N, Real-time identification of liver cancers by using indocyanine green fluorescent imaging, Cancer 115 (11) (2009) 2491–2504. [PubMed: 19326450]

[56]. Uchiyama K, Ueno M, Ozawa S, Kiriyama S, Shigekawa Y, Yamaue H, Combined use of contrast-enhanced intraoperative ultrasonography and a fluorescence navigation system for identifying hepatic metastases, World J. Surg 34 (12) (2010) 2953–2959. [PubMed: 20734045]

[57]. Gotoh K, Yamada T, Ishikawa O, Takahashi H, Eguchi H, Yano M, Ohigashi H, Tomita Y, Miyamoto Y, Imaoka S, A novel image-guided surgery of hepatocellular carcinoma by indocyanine green fluorescence imaging navigation, J. Surg. Oncol 100 (1) (2009) 75–79. [PubMed: 19301311]

[58]. Watanabe M, Tsunoda A, Narita K, Kusano M, Miwa M, Colonic tattooing using fluorescence imaging with light-emitting diode-activated indocyanine green: a feasibility study, Surg. Today 39 (3) (2009) 214–218. [PubMed: 19280280]

[59]. Poellinger A, Burock S, Grosenick D, Hagen A, Lüdemann L, Diekmann F, Engelken F, Macdonald R, Rinneberg H, Schlag P-M, Breast cancer: early- and late-fluorescence near-infrared imaging with indocyanine greenda preliminary study, Radiol 258 (2) (2011) 409–416.

[60]. Kimura T, Muguruma N, Ito S, Okamura S, Imoto Y, Miyamoto H, Kaji M, Kudo E, Infrared fluorescence endoscopy for the diagnosis of superficial gastric tumors, Gastrointest. Endosc 66 (1) (2007) 37–43. [PubMed: 17591472]

[61]. Iseki K, Tatsuta M, Iishi H, Sakai N, Yano H, Ishiguro S, Effectiveness of the near-infrared electronic endoscope for diagnosis of the depth of involvement of gastric cancers, Gastrointest. Endosc 52 (6) (2000) 755–762. [PubMed: 11115912]

[62]. Intes X, Ripoll J, Chen Y, Nioka S, Yodh A, Chance B, In vivo continuous-wave optical breast imaging enhanced with Indocyanine Green, Med. Phys 30 (6) (2003) 1039–1047. [PubMed: 12852527]

[63]. Alacam B, Yazici B, Intes X, Nioka S, Chance B, Pharmacokinetic-rate images of indocyanine green for breast tumors using near-infrared optical methods, Phys. Med. Biol 53 (4) (2008) 837. [PubMed: 18263944]

[64]. Anderson KE, Bloomer JR, Bonkovsky HL, Kushner JP, Pierach CA, Pimstone NR, Desnick RJ, Recommendations for the diagnosis and treatment of the acute porphyrias, Ann. Intern. Med 142 (6) (2005) 439–450. [PubMed: 15767622]

[65]. Stummer W, Pichlmeier U, Meinel T, Wiestler OD, Zanella F, Reulen H-J, A.-G.S. Group, Fluorescence-guided surgery with 5-aminolevulinic acid for resection of malignant glioma: a randomised controlled multicentre phase III trial, Lancet Oncol 7 (5) (2006) 392–401. [PubMed: 16648043]

[66]. Kriegmair M, Baumgartner R, Knuchel R, Stepp H, Hofstadter F, Hofstetter A, Detection of early bladder cancer by 5-aminolevulinic acid induced porphyrin fluorescence, J. Urol 155 (1) (1996) 105–110. [PubMed: 7490803]

[67]. Kajimoto Y, Kuroiwa T, Miyatake S-I, Ichioka T, Miyashita M, Tanaka H, Tsuji M, Use of 5-aminolevulinic acid in fluorescence-guided resection of meningioma with high risk of recurrence: case report, J. Neurosurg 106 (6) (2007) 1070–1074. [PubMed: 17564181]

[68]. Kennedy J, Pottier R, Pross D, Photodynamic therapy with endogenous protoporphyrin: IX: basic principles and present clinical experience, J. Photochem. Photobiol. B 6 (1–2) (1990) 143–148. [PubMed: 2121931]

[69]. Aminolevulinic acid hydrochloride, Known as ALA HCl (Gleolan, NX Development Corp.) as an Optical Imaging Agent Indicated in Patients with Gliomas, 2017.

[70]. Hyun H, Henary M, Gao T, Narayana L, Owens EA, Lee JH, Park G, Wada H, Ashitate Y, Frangioni JV, 700-nm zwitterionic near-infrared fluorophores for dual-channel image-guided surgery, Mol. Imaging Biol 18 (1) (2016) 52–61. [PubMed: 26084246]

[71]. Choi HS, Gibbs SL, Lee JH, Kim SH, Ashitate Y, Liu F, Hyun H, Park G, Xie Y, Bae S, Targeted zwitterionic near-infrared fluorophores for improved optical imaging, Nat. Biotechnol 31 (2) (2013) 148–153. [PubMed: 23292608]

[72]. Antaris AL, Chen H, Cheng K, Sun Y, Hong G, Qu C, Diao S, Deng Z, Hu X, Zhang B, A small-molecule dye for NIR-II imaging, Nat. Mater 15 (2) (2016) 235–242. [PubMed: 26595119]

[73]. Nicholson R, Gee J, Harper M, EGFR and cancer prognosis, Eur. J. Cancer 37 (2001) 9–15. [PubMed: 11165124]

[74]. Fan Z, Masui H, Altas I, Mendelsohn J, Blockade of epidermal growth factor receptor function by bivalent and monovalent fragments of 225 anti-epidermal growth factor receptor monoclonal antibodies, Cancer Res 53 (18) (1993) 4322–4328. [PubMed: 8364927]

[75]. Rosenthal EL, Kulbersh BD, King T, Chaudhuri TR, Zinn KR, Use of fluorescent labeled anti–epidermal growth factor receptor antibody to image head and neck squamous cell carcinoma xenografts, Mol. Cancer Ther 6 (4) (2007) 1230–1238. [PubMed: 17431103]

[76]. Gleysteen JP, Newman JR, Chhieng D, Frost A, Zinn KR, Rosenthal EL, Fluorescent labeled anti-EGFR antibody for identification of regional and distant metastasis in a preclinical xenograft model, Head neck 30 (6) (2008) 782–789. [PubMed: 18228526]

[77]. Heath CH, Deep NL, Sweeny L, Zinn KR, Rosenthal EL, Use of panitumumab-IRDye800 to image microscopic head and neck cancer in an orthotopic surgical model, Ann. Surg. Oncol 19 (12) (2012) 3879–3887. [PubMed: 22669455]

[78]. Becker A, Hessenius C, Licha K, Ebert B, Sukowski U, Semmler W, Wiedenmann B, Grötzinger C, Receptor-targeted optical imaging of tumors with near-infrared fluorescent ligands, Nat. Biotechnol 19 (4) (2001) 327–331. [PubMed: 11283589]

[79]. Ke S, Wen X, Gurfinkel M, Charnsangavej C, Wallace S, Sevick-Muraca EM, Li C, Near-infrared optical imaging of epidermal growth factor receptor in breast cancer xenografts, Cancer Res 63 (22) (2003) 7870–7875. [PubMed: 14633715]

[80]. Sandoval RM, Kennedy MD, Low PS, Molitoris BA, Uptake and trafficking of fluorescent conjugates of folic acid in intact kidney determined using intravital two-photon microscopy, Am. J. Physiol. Cell Physiol 287 (2) (2004) C517–C526. [PubMed: 15102609]

[81]. Veiseh M, Gabikian P, Bahrami S-B, Veiseh O, Zhang M, Hackman RC, Ravanpay AC, Stroud MR, Kusuma Y, Hansen SJ, Tumor paint: a chlorotoxin: Cy5. 5 bioconjugate for intraoperative visualization of cancer foci, Cancer Res 67 (14) (2007) 6882–6888. [PubMed: 17638899]

[82]. Van Dam GM, Themelis G, Crane LM, Harlaar NJ, Pleijhuis RG, Kelder W, Sarantopoulos A, De Jong JS, Arts HJ, Van Der Zee AG, Intraoperative tumor-specific fluorescence imaging in ovarian cancer by folate receptor-[alpha] targeting: first in-human results, Nat. Med 17 (10) (2011) 1315–1319. [PubMed: 21926976]

[83]. Thariat J, Etienne-Grimaldi M-C, Grall D, Bensadoun R-J, Cayre A, Penault-Llorca F, Veracini L, Francoual M, Formento J-L, Dassonville O, Epidermal growth factor receptor protein detection in head and neck cancer patients: a many-faceted picture, Clin. Cancer Res 18 (5) (2012) 1313–1322. [PubMed: 22228639]

[84]. Ang KK, Berkey BA, Tu X, Zhang H-Z, Katz R, Hammond EH, Fu KK, Milas L, Impact of epidermal growth factor receptor expression on survival and pattern of relapse in patients with advanced head and neck carcinoma, Cancer Res 62 (24) (2002) 7350–7356. [PubMed: 12499279]

[85]. Sun JY, Shen J, Thibodeaux J, Huang G, Wang Y, Gao J, Low PS, Dimitrov DS, Sumer BD, In vivo optical imaging of folate receptor-b in head and neck squamous cell carcinoma, Laryngoscope 124 (8) (2014).

[86]. Cai W, Shin D-W, Chen K, Gheysens O, Cao Q, Wang SX, Gambhir SS, Chen X, Peptide-labeled near-infrared quantum dots for imaging tumor vasculature in living subjects, Nano Lett 6 (4) (2006) 669–676. [PubMed: 16608262]

[87]. Lidke DS, Nagy P, Heintzmann R, Arndt-Jovin DJ, Post JN, Grecco HE, Jares-Erijman EA, Jovin TM, Quantum dot ligands provide new insights into erbB/HER receptor–mediated signal transduction, Nat. Biotechnol 22 (2) (2004) 198–203. [PubMed: 14704683]

[88]. Gao X, Cui Y, Levenson RM, Chung LW, Nie S, In vivo cancer targeting and imaging with semiconductor quantum dots, Nat. Biotechnol 22 (8) (2004) 969–976. [PubMed: 15258594]

[89]. Kim S, Fisher B, Eisler H-J, Bawendi M, Type-II quantum dots: CdTe/CdSe (core/shell) and CdSe/ZnTe (core/shell) heterostructures, J. Am. Chem. Soc 125 (38) (2003) 11466–11467. [PubMed: 13129327]

[90]. Bailey RE, Nie S, Alloyed semiconductor quantum dots: tuning the optical properties without changing the particle size, J. Am. Chem. Soc 125 (23) (2003) 7100–7106. [PubMed: 12783563]

[91]. Kim S, Lim YT, Soltesz EG, De Grand AM, Lee J, Nakayama A, Parker JA, Mihaljevic T, Laurence RG, Dor DM, Near-infrared fluorescent type II quantum dots for sentinel lymph node mapping, Nat. Biotechnol 22 (1) (2004) 93–97. [PubMed: 14661026]

[92]. So M.-k., Xu C, Loening AM, Gambhir SS, Rao J, Self-illuminating quantum dot conjugates for in vivo imaging, Nat. Biotechnol 24 (3) (2006) 339–343. [PubMed: 16501578]

[93]. Lin C-AJ, Yang T-Y, Lee C-H, Huang SH, Sperling RA, Zanella M, Li JK, Shen J-L, Wang H-H, Yeh H-I, Synthesis, characterization, and bioconjugation of fluorescent gold nanoclusters toward biological labeling applications, ACS Nano 3 (2) (2009) 395–401. [PubMed: 19236077]

[94]. Wang C, Li J, Amatore C, Chen Y, Jiang H, Wang XM, Gold nanoclusters and graphene nanocomposites for drug delivery and imaging of cancer cells, Angew Chem Int. Ed 50 (49) (2011) 11644–11648.

[95]. Wang J, Zhang G, Li Q, Jiang H, Liu C, Amatore C, Wang X, In vivo self-bio-imaging of tumors through in situ biosynthesized fluorescent gold nanoclusters, Sci. Rep 3 (2013) 1157. [PubMed: 23362457]

[96]. Gao S, Chen D, Li Q, Ye J, Jiang H, Amatore C, Wang X, Near-infrared fluorescence imaging of cancer cells and tumors through specific biosynthesis of silver nanoclusters, Sci. Rep 4 (2014) 4384. [PubMed: 24632892]

[97]. Wu X, He X, Wang K, Xie C, Zhou B, Qing Z, Ultrasmall near-infrared gold nanoclusters for tumor fluorescence imaging in vivo, Nanoscale 2 (10) (2010) 2244–2249. [PubMed: 20835443]

[98]. Welsher K, Liu Z, Sherlock SP, Robinson JT, Chen Z, Daranciang D, Dai H, A route to brightly fluorescent carbon nanotubes for near-infrared imaging in mice, Nat. Nanotechnol 4 (11) (2009) 773–780. [PubMed: 19893526]

[99]. Robinson JT, Welsher K, Tabakman SM, Sherlock SP, Wang H, Luong R, Dai H, High performance in vivo near-IR (> 1 μm) imaging and photothermal cancer therapy with carbon nanotubes, Nano Res 3 (11) (2010) 779–793. [PubMed: 21804931]

[100]. Robinson JT, Hong G, Liang Y, Zhang B, Yaghi OK, Dai H, In vivo fluorescence imaging in the second near-infrared window with long circulating carbon nanotubes capable of ultrahigh tumor uptake, J. Am. Chem. Soc 134 (25) (2012) 10664–10669. [PubMed: 22667448]

[101]. Palner M, Pu K, Shao S, Rao J, Semiconducting polymer nanoparticles with persistent near-infrared luminescence for in vivo optical imaging, Angew. Chem 127 (39) (2015) 11639–11642.

[102]. Nakajima T, Mitsunaga M, Bander NH, Heston WD, Choyke PL, Kobayashi H, Targeted, activatable, in vivo fluorescence imaging of Prostate-specific Membrane Antigen (PSMA)-positive tumors using the quenched humanized J591 antibody-ICG conjugate, Bioconjug. Chem 22 (8) (2011) 1700. [PubMed: 21740058]

[103]. Kobayashi H, Ogawa M, Alford R, Choyke PL, Urano Y, New strategies for fluorescent probe design in medical diagnostic imaging, Chem. Rev 110 (5) (2010) 2620. [PubMed: 20000749]

[104]. Urano Y, Sakabe M, Kosaka N, Ogawa M, Mitsunaga M, Asanuma D, Kamiya M, Young MR, Nagano T, Choyke PL, Rapid cancer detection by topically spraying a γ-glutamyltranspeptidase–activated fluorescent probe, Sci. Transl. Med 3 (110) (2011), 110ra119–a11110ra119.

[105]. Asanuma D, Sakabe M, Kamiya M, Yamamoto K, Hiratake J, Ogawa M, Kosaka N, Choyke PL, Nagano T, Kobayashi H, Sensitive β-galactosidase-targeting fluorescence probe for visualizing small peritoneal metastatic tumours in vivo, Nat. Comm 6 (2015).

[106]. Voegtlin C, Kahler H, Fitch R, The estimation of the hydrogen ion concentration of tissues in living animals by means of the capillary glass electrode, Nat. Inst. Hlth Bull 164 (1935) 15–27.

[107]. Urano Y, Asanuma D, Hama Y, Koyama Y, Barrett T, Kamiya M, Nagano T, Watanabe T, Hasegawa A, Choyke PL, Selective molecular imaging of viable cancer cells with pH-activatable fluorescence probes, Nat. Med 15 (1) (2009) 104–109. [PubMed: 19029979]

[108]. Xiong H, Kos P, Yan Y, Zhou K, Miller JB, Elkassih S, Siegwart DJ, Activatable water-soluble probes enhance tumor imaging by responding to dysregulated pH and exhibiting high tumor-to-liver fluorescence emission contrast, Bioconjug. Chem 27 (7) (2016) 1737–1744. [PubMed: 27285307]

[109]. Lee H, Akers W, Bhushan K, Bloch S, Sudlow G, Tang R, Achilefu S, Near-infrared pH-activatable fluorescent probes for imaging primary and metastatic breast tumors, Bioconjug. Chem 22 (4) (2011) 777–784. [PubMed: 21388195]

[110]. Reshetnyak YK, Andreev OA, Segala M, Markin VS, Engelman DM, Energetics of peptide (pHLIP) binding to and folding across a lipid bilayer membrane, Proc. Natl. Acad. Sci. U. S. A 105 (40) (2008) 15340–15345. [PubMed: 18829441]

[111]. Reshetnyak YK, Yao L, Zheng S, Kuznetsov S, Engelman DM, Andreev OA, Measuring tumor aggressiveness and targeting metastatic lesions with fluorescent pHLIP, Mol. Imaging Biol 13 (6) (2011) 1146–1156. [PubMed: 21181501]

[112]. Weerakkody D, Moshnikova A, Thakur MS, Moshnikova V, Daniels J, Engelman DM, Andreev OA, Reshetnyak YK, Family of pH (low) insertion peptides for tumor targeting, Proc. Natl. Acad. Sci. U. S. A 110 (15) (2013) 5834–5839. [PubMed: 23530249]

[113]. Ma X, Wang Y, Zhao T, Li Y, Su L-C, Wang Z, Huang G, Sumer BD, Gao J, Ultra-pH-sensitive nanoprobe library with broad pH tunability and fluorescence emissions, J. Am. Chem. Soc 136 (31) (2014) 11085–11092. [PubMed: 25020134]

[114]. Wang Y, Zhou K, Huang G, Hensley C, Huang X, Ma X, Zhao T, Sumer BD, DeBerardinis RJ, Gao J, A nanoparticle-based strategy for the imaging of a broad range of tumours by nonlinear amplification of microenvironment signals, Nat. Mater 13 (2) (2014) 204–212. [PubMed: 24317187]

[115]. Wang C, Wang Y, Li Y, Bodemann B, Zhao T, Ma X, Huang G, Hu Z, DeBerardinis RJ, White MA, A nanobuffer reporter library for fine-scale imaging and perturbation of endocytic organelles, Nat. Comm 6 (2015) 8524.

[116]. Wang C, Zhao T, Li Y, Huang G, White MA, Gao J, Investigation of endosome and lysosome biology by ultra pH-sensitive nanoprobes, Adv. Drug Deliv. Rev 113 (2017) 87–96. [PubMed: 27612550]

[117]. Zhou K, Wang Y, Huang X, Luby-Phelps K, Sumer BD, Gao J, Tunable, ultrasensitive pH-responsive nanoparticles targeting specific endocytic organelles in living cells, Angew. Chem 123 (27) (2011) 6233–6238.

[118]. Li Y, Zhao T, Wang C, Lin Z, Huang G, Sumer BD, Gao J, Molecular basis of cooperativity in pH-triggered supramolecular self-assembly, Nat. Comm 7 (2016).

[119]. Wang W, Fang H, Groom L, Cheng A, Zhang W, Liu J, Wang X, Li K, Han P, Zheng M, Superoxide flashes in single mitochondria, Cell 134 (2) (2008) 279–290. [PubMed: 18662543]

[120]. Belousov VV, Fradkov AF, Lukyanov KA, Staroverov DB, Shakhbazov KS, Terskikh AV, Lukyanov S, Genetically encoded fluorescent indicator for intracellular hydrogen peroxide, Nat. Methods 3 (4) (2006) 281–286. [PubMed: 16554833]

[121]. Dooley CT, Dore TM, Hanson GT, Jackson WC, Remington SJ, Tsien RY, Imaging dynamic redox changes in mammalian cells with green fluorescent protein indicators, J. Biol. Chem 279 (21) (2004) 22284–22293. [PubMed: 14985369]

[122]. Hempel SL, Buettner GR, O'Malley YQ, Wessels DA, Flaherty DM, Dihydrofluorescein diacetate is superior for detecting intracellular oxidants: comparison with 2′, 7′-dichlorodihydrofluorescein diacetate, 5 (and 6)-carboxy-2′, 7′-dichlorodihydrofluorescein

diacetate, and dihydrorhodamine 123, Free Radic. Biol. Med 27 (1) (1999) 146–159. [PubMed: 10443931]

[123]. Miller EW, Albers AE, Chang CJ, Pralle A, Isacoff EY, Boronate-based fluorescent probes for imaging cellular hydrogen peroxide, J. Am. Chem. Soc 127 (47) (2005) 16652. [PubMed: 16305254]

[124]. Lee D, Khaja S, Velasquez-Castano JC, Dasari M, Sun C, Petros J, Taylor WR, Murthy N, In vivo imaging of hydrogen peroxide with chemiluminescent nanoparticles, Nat. Mater 6 (10) (2007) 765–769. [PubMed: 17704780]

[125]. Pu K, Shuhendler AJ, Jokerst JV, Mei J, Gambhir SS, Bao Z, Rao J, Semiconducting polymer nanoparticles as photoacoustic molecular imaging probes in living mice, Nat. Nanotechnol 9 (3) (2014) 233–239. [PubMed: 24463363]

[126]. 5-Aminolevulinic Acid (GLEOLAN), 1999.

[127]. Yu D, Gustafson WC, Han C, Lafaye C, Noirclerc-Savoye M, Ge W-P, Thayer DA, Huang H, Kornberg TB, Royant A, An improved monomeric infrared fluorescent protein for neuronal and tumor brain imaging, Nat. Comm 5 (2014) 3626.

[128]. Shcherbakova DM, Baloban M, Emelyanov AV, Brenowitz M, Guo P, Verkhusha VV, Bright monomeric near-infrared fluorescent proteins as tags and biosensors for multiscale imaging, Nat. Comm 7 (2016).

[129]. Schwarzl€ander M, Logan DC, Fricker MD, Sweetlove LJ, The circularly permuted yellow fluorescent protein cpYFP that has been used as a superoxide probe is highly responsive to pH but not superoxide in mitochondria: implications for the existence of superoxide ‘flashes’, Biochem. J 437 (3) (2011) 381–387. [PubMed: 21631430]

[130]. Fang H, Chen M, Ding Y, Shang W, Xu J, Zhang X, Zhang W, Li K, Xiao Y, Gao F, Imaging superoxide flash and metabolism-coupled mitochondrial permeability transition in living animals, Cell Res 21 (9) (2011) 1295–1304. [PubMed: 21556035]

[131]. Hanson GT, Aggeler R, Oglesbee D, Cannon M, Capaldi RA, Tsien RY, Remington SJ, Investigating mitochondrial redox potential with redox-sensitive green fluorescent protein indicators, J. Biol. Chem 279 (13) (2004) 13044–13053. [PubMed: 14722062]

[132]. Ermakova YG, Bilan DS, Matlashov ME, Mishina NM, Markvicheva KN, Subach OM, Subach FV, Bogeski I, Hoth M, Enikolopov G, Red fluorescent genetically encoded indicator for intracellular hydrogen peroxide, Nat. Comm 5 (2014) 5222.

[133]. Welsher K, Sherlock SP, Dai H, Deep-tissue anatomical imaging of mice using carbon nanotube fluorophores in the second near-infrared window, Proc. Natl. Acad. Sci. U. S. A 108 (22) (2011) 8943–8948. [PubMed: 21576494]

[134]. Hong G, Diao S, Chang J, Antaris AL, Chen C, Zhang B, Zhao S, Atochin DN, Huang PL, Andreasson KI, Through-skull fluorescence imaging of the brain in a new near-infrared window, Nat. Photonics 8 (9) (2014) 723–730. [PubMed: 27642366]

[135]. Tonn J-C, Stummer W, Fluorescence-guided resection of malignant gliomas using 5-aminolevulinic acid: practical use, risks, and pitfalls, Clin. Neurosurg 55 (3) (2008) 20–26. [PubMed: 19248665]

[136]. Antaris AL, Chen H, Diao S, Ma Z, Zhang Z, Zhu S, Wang J, Lozano AX, Fan Q, Chew L, A high quantum yield molecule-protein complex fluorophore for near-infrared II imaging, Nat. Comm 8 (2017).

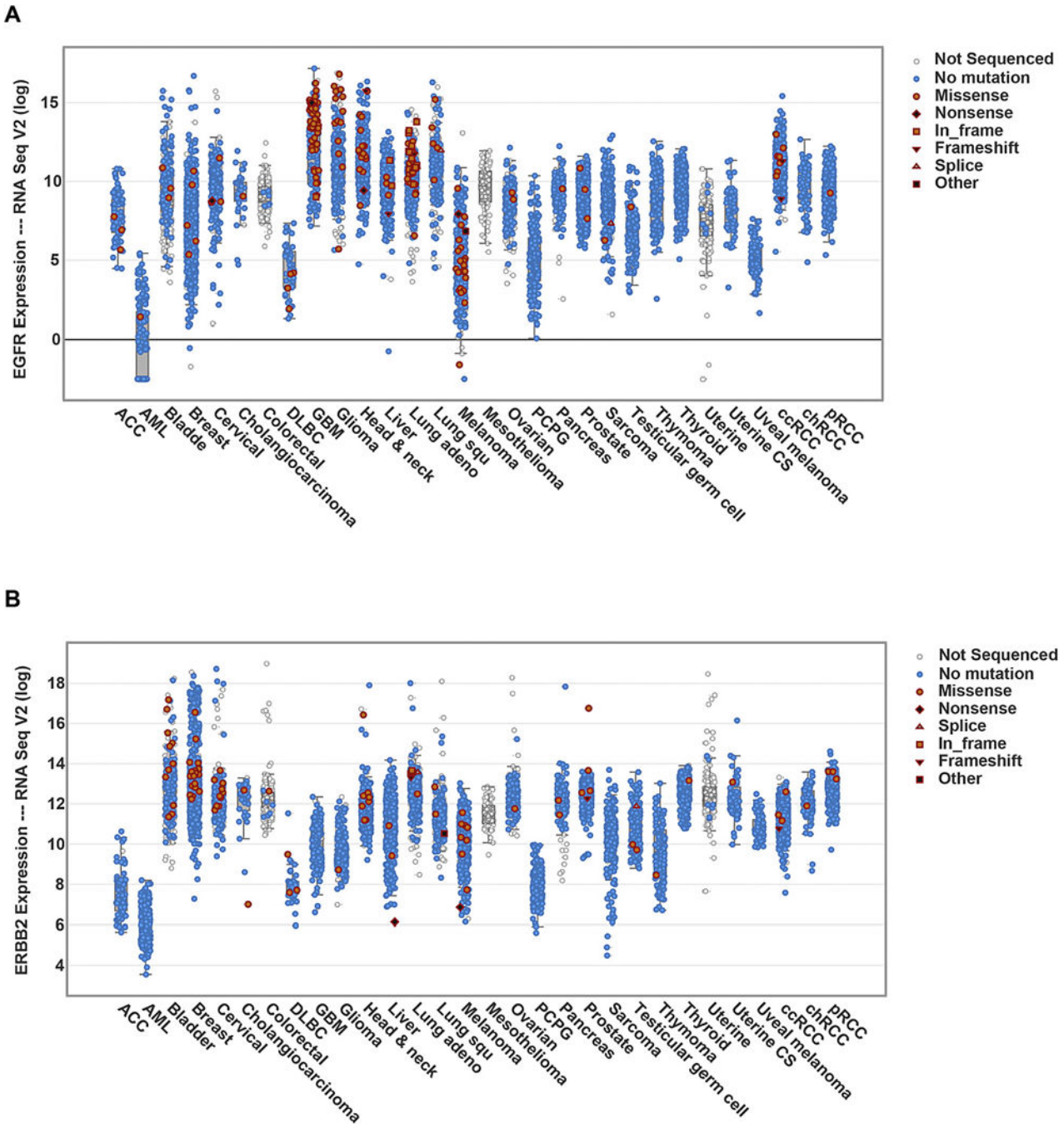

Fig. 1.

Summary of *EGFR* (**A**) and *ERBB2* (*HER2*) (**B**) expressions across multiple cancer types. The data are from RNA sequencing results of patient samples, which may not directly correlate with protein expression levels. Abbreviations: ACC (Adrenocortical carcinoma), AML (Acute Myeloid Leukemia), DLBC (Lymphoid neoplasm diffuse large B-cell lymphoma), GBM (Glioblastoma multiforme), Lung adeno (Lung adenocarcinoma), Lung squ (Lung squamous cell carcinoma), PCPG (Pheochromocytoma and Paraganglioma), Uterine CS (Uterine carcinosarcoma), ccRCC (Clear cell renal cell carcinoma), chRCC

(Chromophobe renal cell carcinoma), pRCC(Papillary renal cell carcinoma). Adapted from data source: The Cancer Genomics Atlas (TCGA) as of May 2017.

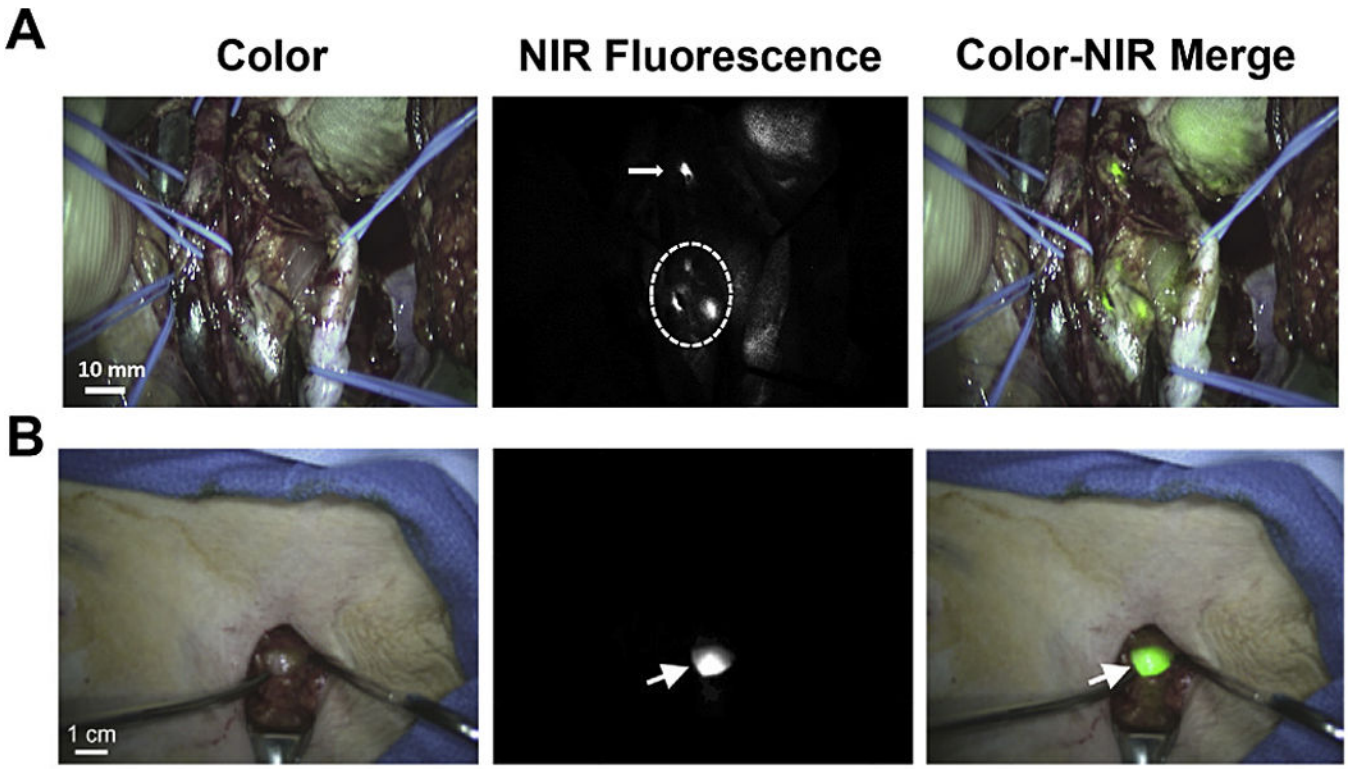

Fig. 2. Methylene blue and ICG for *in vivo* NIR fluorescence imaging.

(**A**) Intraoperative NIR imaging of the surgical field. A bright fluorescent signal within the dashed circle identified the location of the bulk of the tumor. A small lesion was also identified ~5 cm away from the main lesion (arrow). (**B**) Intraoperative sentinel lymph node (arrow) mapping in the axilla of a woman with breast cancer after peri-tumoral injection of ICG-human serum albumin. Adapted from Refs. [47 and 49]with permissions.

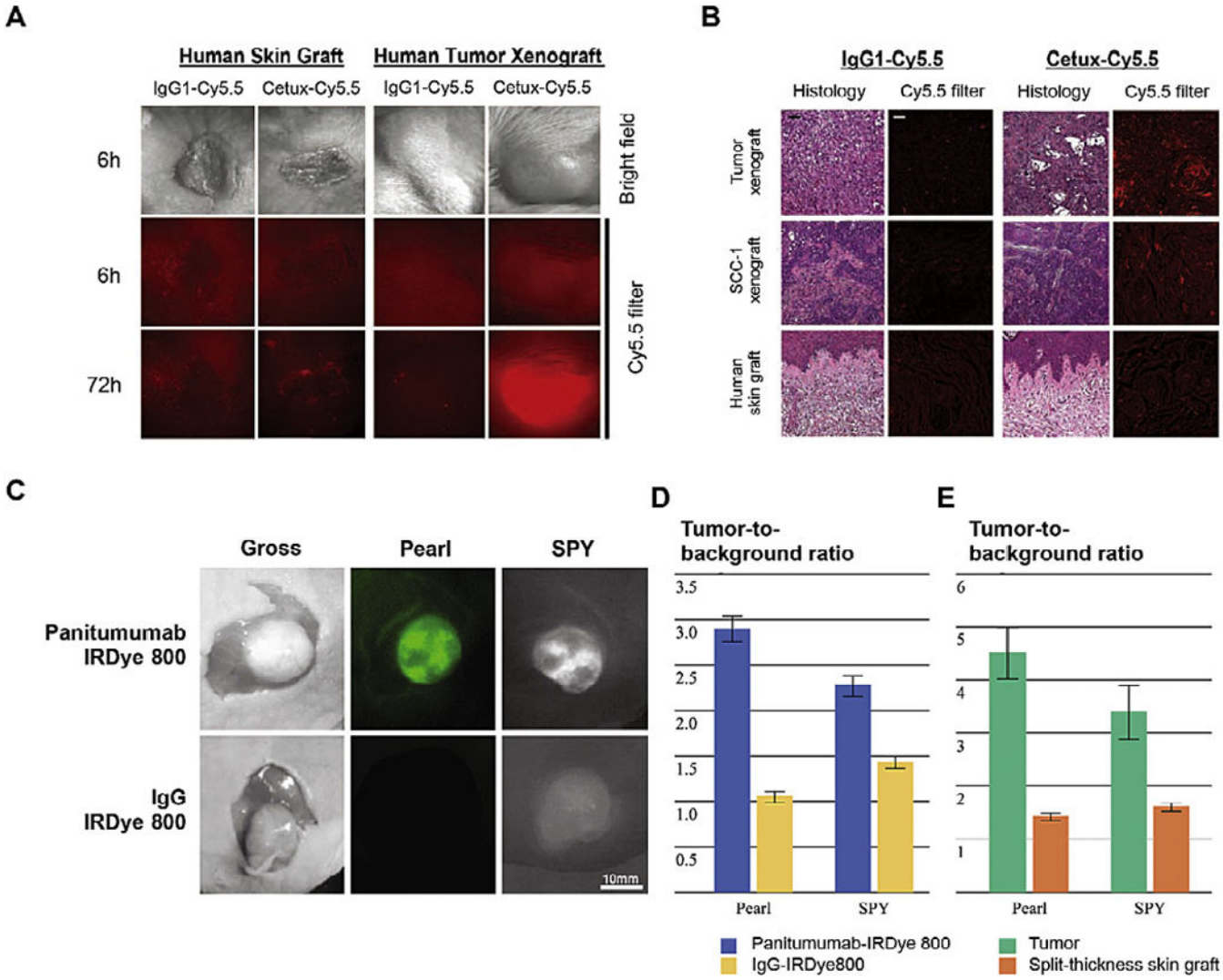

Fig. 3. Antibody-dye conjugates in tumor imaging.

(**A**) Stereomicroscopic imaging of engrafted human skin xenografts and human tumor explant xenografts in SCID mice injected with cetuximab conjugated with Cy5.5 (Cetux-Cy5.5) or nonspecific human IgG1 antibody (IgG1-Cy5.5). (**B**) Head-to-head comparison of the histology and fluorescent results in tumor sections. (**C**) Uptake of panitumumab-IRDye800 versus non-specific IgG-IRDye 800 using the Pearl and SPY Systems in mice with flank SCC1 tumors. (**D**) The tumor-to-background ratio in mice injected with panitumumab-IRDye800 or IgG-IRDye800. (**E**) Panitumumab-IRDye800 demonstrated significantly higher fluorescent signal in the tumor than the split-thickness skin graft in both the Pearl and SPY imager. Adapted from Refs. [75 and 77] with permissions.

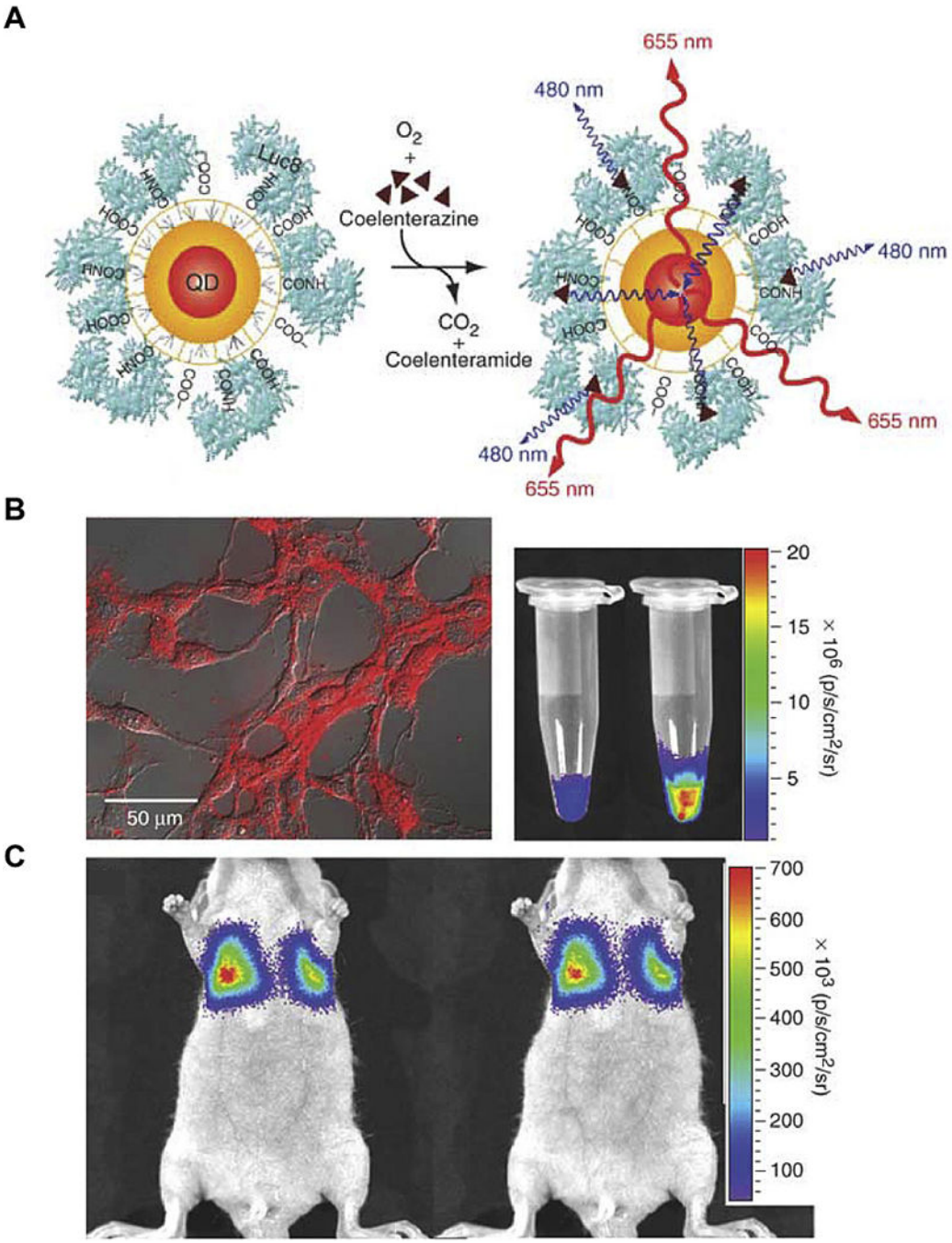

Fig. 4. Self-illuminating QDs for *in vivo* tumor imaging.

(**A**) The design of a QD conjugated with a BRET donor Luc8. The energy transferred from Lu8-induced oxidation of coelenterazine results in QD emission. (**B**) Illumination of C6 glioma cells by QD655-Luc8-R9. (**C**) Representative images of nude mice injected with labeled cells via tail vein. Adapted from Ref. [92] with permissions.

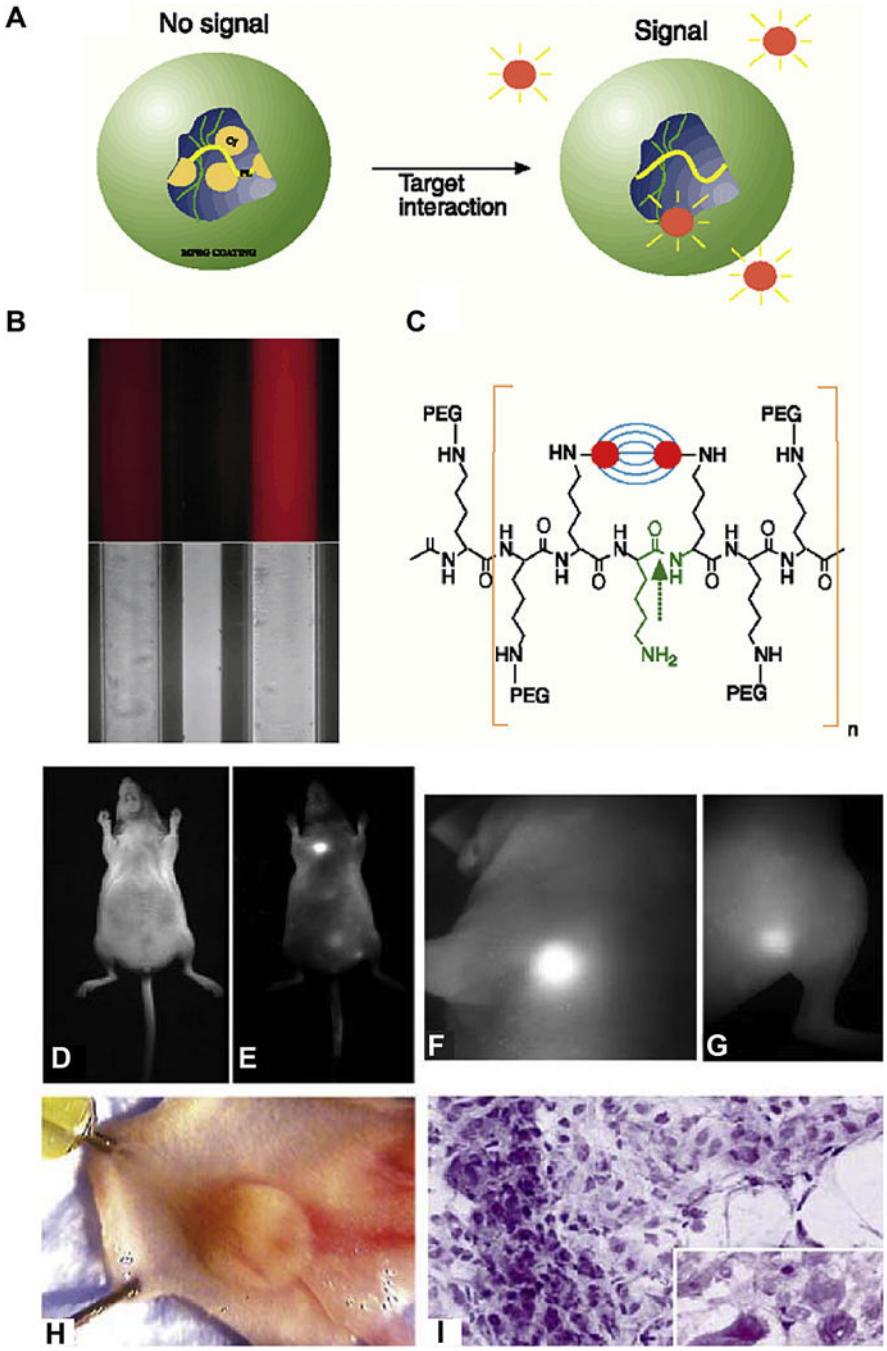

Fig. 5. A protease-activated NIR imaging agent for tumor detection *in vivo*.

(**A**) The mechanistic illustration of nanoprobe activation. In the absence of enzymes, the proximity of fluorochromes to each other leads to the initial fluorescence quenching. (**B**) Fluorescent and bright-light image of the nanoprobe before (left) and after (right) activation. (**C**) Chemical structure of the copolymers used in the nanoprobe design. Bright-light and fluorescent images of LX-1 tumor implanted to the mammary fat pad of a nude mice were shown in (**D**) and (**E**); while high-resolution fluorescent images of the tumor and an additional thigh tumor were shown in (**F**) and (**G**). (**H**) Dissected tumor from mammary fat

pad. (I) Histology staining of the fluorescence-positive tumors. Adapted from Ref. [22] with permissions.

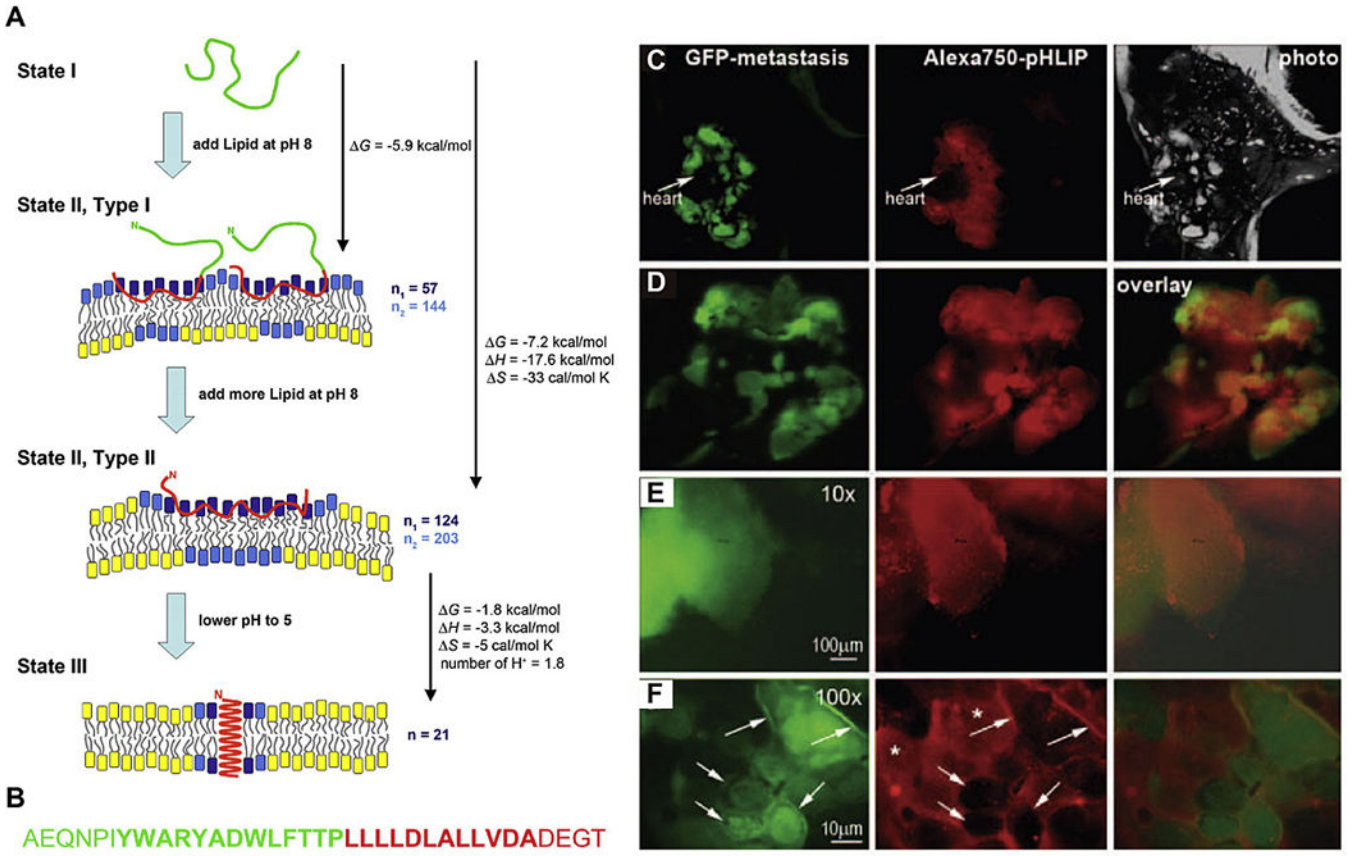

Fig. 6. Targeting tumor metastasis with fluorescent pHLIP™.

(**A**) Schematic showing the mechanism of pH-sensitive folding and insertion of pHLIP™ into a lipid bilayer membrane. (**B**) The amino acid sequence of pHLIP™. (**C**) Whole-body imaging of a GFP-labeled metastatic M4A4 tumor in lungs. (**D**) GFP and NIR fluorescence overlay. 10 × and 100 × magnification of GFP and NIR fluorescent images were shown in (**E**) and (**F**). Adapted from Refs. [110] and [111] with permissions.

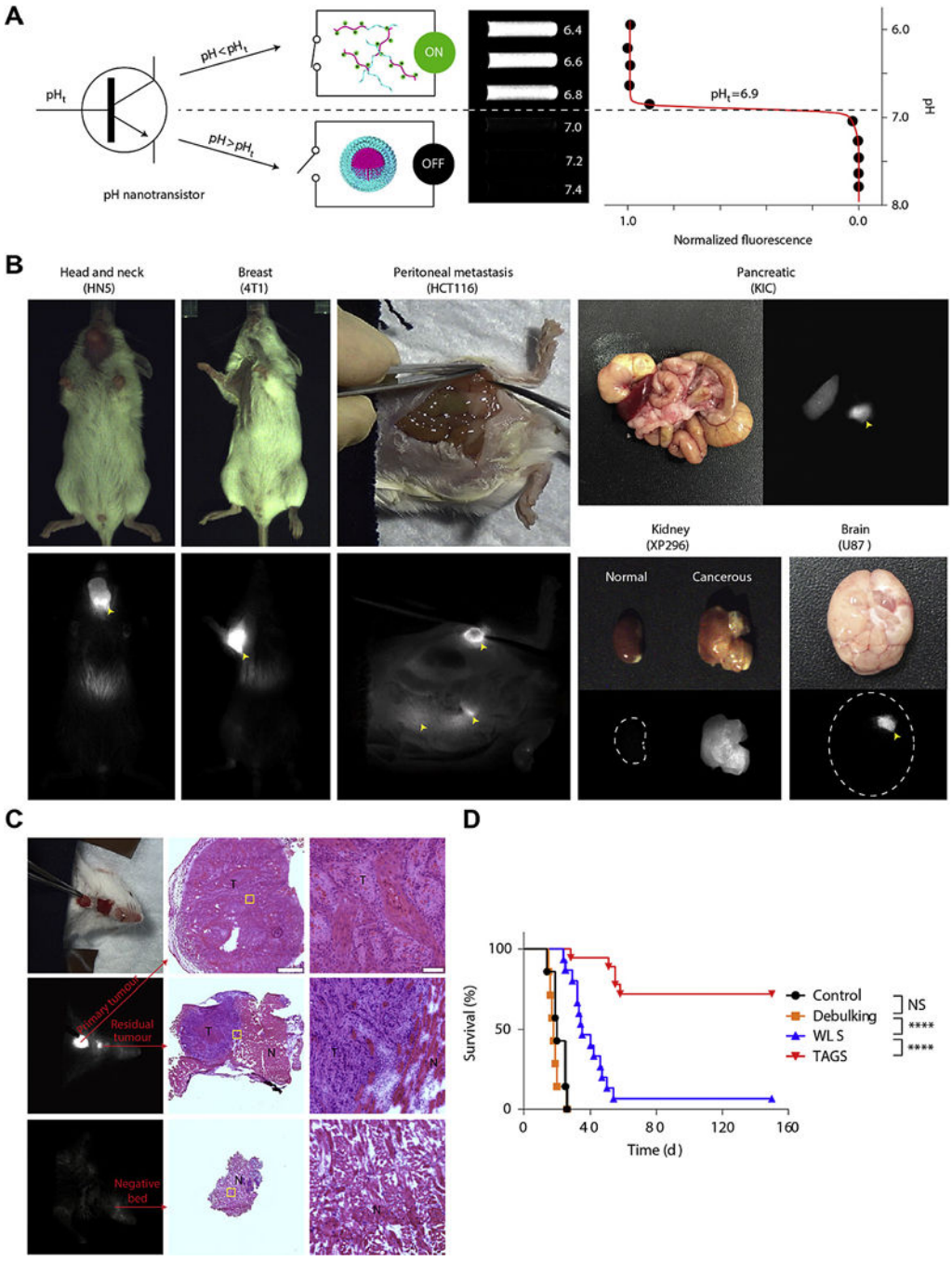

Fig. 7. A transistor-like pH nanoprobe for tumor detection and image-guided surgery.

(**A**) A transistor-like design of ICG-UPS nanoprobe with binary off/on fluorescent response at the transition pH of 6.9. (**B**) Imaging of a variety of tumor models 24 h after injection of ICG-UPS nanoprobes by using SPY Elite clinical camera. Yellow arrowheads indicate the location of tumors. (**C**) Successful surgical resection of primary and residual HN5 tumors as validated by histology. (**D**) Long-term survival curves of mice with debulking surgery, white-light surgery (WLS), tumor-acidosis-guided surgery (TAGS) or without surgery.

Adapted from Ref. [20]with permissions. (For interpretation of the references to colour in this figure legend, the reader is referred to the web version of this article.)

Table 1

Summary of common fluorescent imaging probes for optical tumor imaging.

Category	Examples	Excitation/Emission	Properties	Phase	Pros	Cons	Refs
Small molecules	Indocyanine green (ICG)	805/835 nm (in whole blood)	Negatively charged; hydrophobic; always-ON	FDA-approved	Easy tissue penetration; fast systemic clearance	Low tissue accumulation; limited imaging payload; non-specific binding	[49–53]
	Methylene blue (MB)	665/686 nm	Positively charged; hydrophilic; always-ON	FDA-approved			[46–48]
	5-ALA	407/635 and 705 nm (protoporphyrin IX)	Responsive to reduced activity of ferrochelatases in tumor microenvironment	FDA-approved			[64.68,126]
	γ-glutamyl-hydroxymethyl rhodamine green	502/527 nm	Responsive to overexpressed in TME	Pre-clinical			[24]
Fluorescent proteins	IFP2.0 and miRFP709	690/711 nm (IFP2.0); 683/709 nm (miRFP709)	NIR fluorescent proteins that can be endogenously expressed; always-ON	Pre-clinical	High specificity and low signal background	May not be translatable into human	[127,128]
	cpYFP, HyPer and roGFP	420/516 nm (cpYFP); 500/516 nm (HyPer); 405 and 488/510 nm (roGFP)	Fluorescent proteins that are ROS sensitive and can be endogenously expressed	Pre-clinical			[129–132]
Biomolecule-conjugates	cRGD-ZW800–1 conjugate	772/788 nm	Targeting αvβ3; always-ON	Phase I	Active targeting; standard Manufacturing process	Long bloodcirculation time; limited imaging payload	[70,71]
	Panitumumab-IRDye 800 C W conjugate	774/789 nm	Targeting EGFR; always-ON	Phase I			[77]
	Folate-FITC	495/519 nm	Targeting folate receptor α; always-ON	Phase I			[80] [82],
	CH1055-*anti*-EGFR affibody	808/1055 nm	Targeting EGFR; NIR-II window; always-ON	Pre-clinical			[72]
	Trastuzumab conjugated with aniline-BODIPY-based fluorophores	493/503 nm (BODIPY)	Targeting EGFR; pH-responsive	Pre-clinical			[15]
	pHLIP™-Cy5.5/ICG	684/710 nm (Cy5.5); 805/835 nm (ICG)	pH-responsive	Pre-clinical			[110] [111]
Nanoparticulate agents	CdTe/CdSe type-II QDs and alloyed semiconductor QDs	Declining absorption/up to 850 nm	NIR window; can be conjugated with targeting ligands; always-ON	Pre-clinical	Tunable size; high imaging payload	Long bloodcirculation time; non-specificbinding; safety concerns	[91]
	Single-walled carbon nanotubes	550–1000/950–1800 nm	NIR II window; can be conjugated with targeting ligands; always-ON	Pre-clinical			[98–100,133,134]
	Enzyme-activatable copolymers	Dependent on conjugated fluorophores	Responsive to overexpressed proteases in tumor microenvironment	Pre-clinical	Tunable size; high imaging payload; active targeting		[22]

Category	Examples	Excitation/Emission	Properties	Phase	Pros	Cons	Refs
	pH-responsive conjugated copolymers	Dependent on conjugated fluorophores	Responsive to acidic pH in tumor microenvironment	Pre-clinical			[113,114,117]
	Semiconducting polymer conjugated with ROS- and RNS-sensitive dyes	580/680 or 820 nm (Fluorescence resonance energy transfer, RNS-sensitive); NA/680–820 nm (Chemiluminescence resonance energy transfer, ROS-sensitive)	Applicable to high ROS and RNS levels in TME	Pre-clinical			[125]
	Hypoxia-responsive iridium (III) complex conjugated polymer	510/565 and 710 nm	Responsive to increased oxygen consumption in TME; water-soluble	Pre-clinical			[21]